The Astrophysical Journal, 748:106 (21pp), 2012 April 1 doi:10.1088/0004-637X/748/2/106

WHAT CAN WE LEARN ABOUT SOLAR CORONAL MASS EJECTIONS, CORONAL DIMMINGS, AND EXTREME-ULTRAVIOLET JETS THROUGH SPECTROSCOPIC OBSERVATIONS?

Hui Tian[1], Scott W. McIntosh[1], Lidong Xia[2], Jiansen He[3], and Xin Wang[1,3]
[1] High Altitude Observatory, National Center for Atmospheric Research, P.O. Box 3000, Boulder, CO 80307, USA; htian@ucar.edu
[2] Shandong Provincial Key Laboratory of Optical Astronomy and Solar-Terrestrial Environment, School of Space Science and Physics, Shandong University at Weihai, Weihai 264209, China
[3] School of Earth and Space Sciences, Peking University, Beijing 100871, China
Received 2011 November 14; accepted 2012 January 23; published 2012 March 13

ABSTRACT

Solar eruptions, particularly coronal mass ejections (CMEs) and extreme-ultraviolet (EUV) jets, have rarely been investigated with spectroscopic observations. We analyze several data sets obtained by the EUV Imaging Spectrometer on board *Hinode* and find various types of flows during CMEs and jet eruptions. CME-induced dimming regions are found to be characterized by significant blueshift and enhanced line width by using a single Gaussian fit, while a red–blue (RB) asymmetry analysis and an RB-guided double Gaussian fit of the coronal line profiles indicate that these are likely caused by the superposition of a strong background emission component and a relatively weak (∼10%), high-speed (∼100 km s^{-1}) upflow component. This finding suggests that the outflow velocity in the dimming region is probably of the order of 100 km s^{-1}, not ∼20 km s^{-1} as reported previously. These weak, high-speed outflows may provide a significant amount of mass to refill the corona after the eruption of CMEs, and part of them may experience further acceleration and eventually become solar wind streams that can serve as an additional momentum source of the associated CMEs. Density and temperature diagnostics of the dimming region suggest that dimming is primarily an effect of density decrease rather than temperature change. The mass losses in dimming regions as estimated from different methods are roughly consistent with each other, and they are 20%–60% of the masses of the associated CMEs. With the guide of RB asymmetry analysis, we also find several temperature-dependent outflows (speed increases with temperature) immediately outside the (deepest) dimming region. These outflows may be evaporation flows that are caused by the enhanced thermal conduction or nonthermal electron beams along reconnecting field lines, or induced by the interaction between the opened field lines in the dimming region and the closed loops in the surrounding plage region. In an erupted CME loop and an EUV jet, profiles of emission lines formed at coronal and transition region temperatures are found to exhibit two well-separated components, an almost stationary component accounting for the background emission and a highly blueshifted (∼200 km s^{-1}) component representing emission from the erupting material. The two components can easily be decomposed through a double Gaussian fit, and we can diagnose the electron density, temperature, and mass of the ejecta. Combining the speed of the blueshifted component and the projected speed of the erupting material derived from simultaneous imaging observations, we can calculate the real speed of the ejecta.

Key words: line: profiles – solar wind – Sun: corona – Sun: coronal mass ejections (CMEs) – Sun: flares

Online-only material: animations, color figures

1. INTRODUCTION

Coronal mass ejections (CMEs) are large-scale solar eruptions and earth-directed CMEs are often sources of strong geomagnetic storms (e.g., Gosling et al. 1991; Wang et al. 2002, 2006; Zhang & Low 2005; Feng et al. 2009; Liu et al. 2010). Recent statistical studies of Reinard & Biesecker (2008) and Bewsher et al. (2008) have shown that more than 50% of the frontside CMEs are associated with coronal dimmings (or transient coronal holes), which are characterized by abruptly reduced emission in extreme-ultraviolet (EUV) and soft X-rays (e.g., Rust & Hildner 1976; Gopalswamy & Hanaoka 1998; Thompson et al. 1998; Zarro et al. 1999; Zhou et al. 2003; De Toma et al. 2005; McIntosh et al. 2007; Miklenic et al. 2011). Dimmings may mark locations of the footpoints of ejected flux ropes (e.g., Webb et al. 2000) or formed by reconnection between the erupting field and the surrounding magnetic structures (e.g., Attrill et al. 2007; Mandrini et al. 2007). There are basically two types of dimmings: small-scale dimmings associated with the two ends of a pre-CME sigmoid structure (e.g., Sterling & Hudson 1997; Hudson et al. 1998; Zarro et al. 1999; Webb et al. 2000; Jiang et al. 2003; Cheng et al. 2010) and global-scale dimmings, which are often immediately preceded by global "EUV waves" (e.g., Thompson et al. 2000; Attrill et al. 2007). Complete recovery of dimmings may last for hours or days after the eruption of the associated CMEs.

Jet-like phenomena are small-scale solar eruptions and are often observed in X-ray, EUV, and white light. Most jets are associated with small flares (Madjarska et al. 2007). EUV jets are characterized by nearly collimated high-speed motions of plasma at coronal and transition region (TR) temperatures (e.g., Alexander et al. 1999; Lin et al. 2006; Liu et al. 2011; Shen et al. 2011, 2012; Srivastava & Murawski 2011). Studies have shown that EUV jets and X-ray jets are closely associated with each other (Kim et al. 2007; Chifor et al. 2008a; He et al. 2010a; Yang et al. 2011). Recent observations by the Atmospheric Imaging Assembly (AIA; Lemen et al. 2011) on board the *Solar Dynamics Observatory* (*SDO*) have revealed that fine-scale EUV jets (high-speed outflows) are ubiquitous on the Sun (De Pontieu et al. 2011; Tian et al. 2011b; Yang et al. 2011).

Kinematics associated with CMEs and EUV jets are usually studied through coronagraph and broadband observations.

The high cadence and large field of view (FOV) of these imaging observations have greatly enhanced our understanding of these solar eruptions. However, imaging observations only allow us to study the plane of sky (POS) component of the kinematics, which is usually a good approximation of the full kinematics only for limb events. For earth-directed eruptions, especially halo CMEs, which are the cause of most strong geomagnetic storms, imaging instruments placed close to the Sun–Earth line often fail to observe their initial or complete evolution. Spectroscopic observations, on the other hand, can provide information on the plasma motions in the line-of-sight (LOS) direction and thus are critical for us to understand the kinematics of earth-directed eruptions. For both disk and limb eruptions, their three-dimensional evolution can in principle be revealed through simultaneous imaging and spectroscopic observations. In addition, spectra of different emission lines can be used to diagnose plasma properties such as electron density and temperature. Spectroscopic data can also be used to estimate the mass of the erupted material and mass loss in the dimming region.

So far there are only a few spectroscopic investigations of CMEs, dimmings, and EUV jets in the literature. Using observations by the Coronal Diagnostic Spectrometer (CDS; Harrison et al. 1995) on board the *Solar and Heliospheric Observatory* (*SOHO*), Harra & Sterling (2001) reported significant blueshift of emission lines formed at coronal and TR temperatures in dimming regions. This result has been confirmed by recent high-resolution observations of the EUV Imaging Spectrometer (EIS; Culhane et al. 2007) on board *Hinode* (Harra et al. 2007; Jin et al. 2009; Attrill et al. 2010; Chen et al. 2010; Harra et al. 2011a). Blueshift was also found in footpoint regions of small-scale erupted loops (He et al. 2010a). However, a preliminary study by McIntosh et al. (2010) suggests that some line profiles in the dimming regions are asymmetric, with a weak enhancement in the blue wings. EIS observations have also revealed an obvious increase of the line broadening in dimming regions, which was interpreted as a growth of Alfvén wave amplitude or inhomogeneities of flow velocities along the LOS (McIntosh 2009; Chen et al. 2010; Dolla & Zhukov 2011). The presence of asymmetric line profiles suggests that there are probably two emission components and that a single Gaussian fit (SGF) may not reveal the real physics in dimming regions (McIntosh et al. 2010; Dolla & Zhukov 2011).

The outflow speed derived from an SGF is roughly in the range of 10–40 km s^{-1} and usually does not change significantly for coronal emission lines formed at different temperatures (Harra et al. 2007; Jin et al. 2009; Attrill et al. 2010; Chen et al. 2010). However, Imada et al. (2007) reported a temperature-dependent outflow in the dimming region following a CME. The speed of the flow increases from ~10 km s^{-1} at log (T/K) = 4.9 to ~150 km s^{-1} at log (T/K) = 6.3. One-dimensional modeling efforts have been taken to reconstruct this temperature-dependent outflow (Imada et al. 2011).

Line splitting is usually associated with a very high speed (~200 km s^{-1} or larger) plasma motion. Using CDS and EIS observations, Harra & Sterling (2003), Asai et al. (2008), and Li & Ding (2012) found signatures of line splitting indicative of plasma ejection at a speed of ~250 km s^{-1} during CMEs or filament eruptions. Spectra obtained by the Solar Ultraviolet Measurements of Emitted Radiation Spectrograph (Wilhelm et al. 1995; Lemaire et al. 1997) on board *SOHO* have revealed signatures of line splitting associated with the expanding X-ray plasma in a flare/CME event (Innes et al. 2001). Line splitting or obviously blueshifted components have also been found in spectra of EUV jets in coronal holes and active regions (ARs; Wilhelm et al. 2002; Madjarska et al. 2007; Kamio et al. 2007, 2009; Chifor et al. 2008b).

There have been a few investigations of the plasma properties of dimmings and EUV jets. Harrison & Lyons (2000) and Harrison et al. (2003) used the Si x λ347.40 and λ356.04 line pairs to diagnose the electron density and found that it decreased as dimming occurred. Using some assumptions of the emitting volume and the distribution of the amount of material at different temperatures, they also made an effort to estimate the mass loss in the dimming region and found that it is of the same order as the mass of the associated CMEs. Taking values of the formation heights of different emission lines and the densities from static solar atmosphere models, Jin et al. (2009) also developed a method to estimate the mass losses in dimming regions associated with two events during 2006 December 13–15. Using the Fe xii λ186.88 and λ195.12 line pair, Chifor et al. (2008b) measured electron densities higher than log (N_e/cm^{-3}) = 11 for an EUV jet. However, they only simply summed up the spectral intensities in the wavelength windows of the lines and could not separate the blueshifted component from the background emission component.

Besides dimmings and ejecta associated with CMEs and EUV jets, other solar eruption–related phenomena such as flare-induced chromospheric evaporation (Teriaca et al. 2003; Milligan et al. 2006a, 2006b; Milligan & Dennis 2009; Milligan 2011; Del Zanna et al. 2006, 2011b; Chen & Ding 2010; Watanabe et al. 2010; Li & Ding 2011; Graham et al. 2011; Liu et al. 2011), flare-related magnetic reconnection (Wang et al. 2007; Hara et al. 2011), filament oscillations (Chen et al. 2008; Bocchialini et al. 2011), and coronal waves (Harra et al. 2011b; Chen et al. 2011; Veronig et al. 2011) have also been investigated through EUV spectroscopic observations. As we approach the new solar maximum, there is no doubt that more spectroscopic observations will be employed to study solar eruptions since the high-resolution EIS instrument is still in good condition and the Interface Region Imaging Spectrograph (IRIS) is expected to be launched in 2012.

In this paper, we analyze several data sets obtained by EIS during CME eruptions and EUV jets. The shapes of the EIS spectral line profiles suggest that the emission often consists of at least two components so that previous results based on an SGF may need to be reconsidered. We apply the recently improved techniques of red–blue (RB) asymmetry analysis and RB-guided double Gaussian fit (Tian et al. 2011c), which we used previously to study properties of the high-speed outflows in non-eruptive ARs to the spectra acquired during solar eruptions. We find various types of flows and discuss possible mechanisms to produce these flows. We also diagnose the density, temperature, and mass loss (mass) of the dimming region as well as the ejected material. Our analyses demonstrate that EUV spectroscopic observations can provide a lot of valuable information on solar eruptions.

2. OBSERVATIONS, SINGLE GAUSSIAN FIT, AND RB ASYMMETRY ANALYSIS

Table 1 lists some of the observation details of the six events we analyzed. The class and peak time of the associated flare are also listed for each event. There were many fast repetitive rasters (with a scanning cadence of ~6 minutes) for Events 4 and 5, and we only present results for several of them in this paper.

Table 1
EIS Observations Used in This Study

Obs. ID	Scanning Period	Exposure Time (s)	Slit	Flare Class and Peak Time	Remark
1	2006 Dec 14 15:11–16:01	10	1″	X1.5, Dec 14 22:15	CME-related dimming
	2006 Dec 14 19:20–21:35	30			
	2006 Dec 15 01:15–03:30	30			
	2006 Dec 15 04:10–06:25	30			
	2006 Dec 15 10:29–11:19	10			
2	2007 May 19 09:42–10:30	10	1″	B9.5, May 19 13:02	CME-related dimming
	2007 May 19 11:41–15:23	40			
3	2006 Dec 12 19:07–23:46	30	1″	X3.4, Dec 13 02:40	CME-related dimming
	2006 Dec 13 01:12–05:41	30			
4	2011 Jun 21 02:11–05:18	9	2″	C7.7, Jun 21 03:25	CME-related dimming
5	2011 Feb 14 19:13–20:06	8	2″	C6.6, Feb 14 19:30	Erupted CME loop
6	2007 Jun 5 01:51–02:04	5	2″	C1.2, Jun 5 04:23	EUV jet
	2007 Jun 5 04:16–04:29	5			

The flare peak occurred during the EIS scanning period for all events except Event 1, for which the first two scans were done before the occurrence of the associated flare and the last three scans were made 3, 6, and 12 hr, respectively, after the flare peak time.

The SSW routine *eis_prep.pro* was applied to correct and calibrate the EIS data. This includes CCD pedestal and dark current subtraction, cosmic-ray removal, warm and hot pixel identification, absolute calibration, error estimation, and so on. The effects of slit tilt and orbital variation (thermal drift) were estimated by using the SSW routine *eis_wave_corr.pro* and removed from the data. After that, a running average over 3 pixels along the slit was applied to the spectra to improve the signal-to-noise ratio (S/N). Note that Tian et al. (2011c) used the median values of the measurement errors when averaging profiles over several pixels. In this paper, we regard these line profiles as independent measurements of the profile at a single pixel and use the uncertainty propagation theory to calculate the measurement errors for the averaged profile. This usually leads to smaller values of the errors, which is reasonable since the spatial average improves the S/N.

As a common practice, an SGF was applied to each spectrum. The line peak intensity, Doppler shift, and line width can thus be derived. We assume zero shift of the profile averaged over each observation region. We have to mention that the line width can be expressed in different formats and different names are assigned to different formats (e.g., Chae et al. 1998; Peter 2010). A Gaussian line profile can be expressed as

$$I(v) = I_p \exp\left(-\frac{1}{2}\frac{(v-v_0)^2}{\sigma^2}\right), \quad (1)$$

where v, I_p, and v_0 are the wavelength vector (converted into velocity through Doppler effect), peak intensity, and line center, respectively. Chae et al. (1998) defined σ as Gaussian width. The Gaussian width mentioned by Peter (2010) is $\sqrt{2}\sigma$. In Tian et al. (2011c), we followed Peter (2010) and used both the names of Gaussian width and $1/e$ width for $\sqrt{2}\sigma$. To avoid confusion, in the following we use the name exponential width (or $1/e$ width, also used by Peter 2010) instead of Gaussian width for $\sqrt{2}\sigma$.

The technique of RB asymmetry analysis was first introduced by De Pontieu et al. (2009) and is based on a comparison of the two wings of the line profile in the same velocity ranges. The line profile was first interpolated to a spectral resolution 10 times greater than the original one, and then the blue wing emission integrated over a narrow spectral range was subtracted from that over the same range in the red wing. The range of integration was then sequentially stepped outward from the line centroid to build an RB asymmetry profile (simply RB profile). In our previous work (De Pontieu et al. 2009, 2011; De Pontieu & McIntosh 2010; McIntosh & De Pontieu 2009a, 2009b; McIntosh et al. 2011; Tian et al. 2011a; Martínez-Sykora et al. 2011), we used the SGF to determine the line centroid and applied this technique to spectra in coronal holes, quiet Sun, and quiet ARs. Tian et al. (2011c) named this method RB_S, and they further developed two other methods RB_P and RB_D, which are basically the same as RB_S except for the determination of the line centroid. For RB_P, the spectral position corresponding to the peak intensity is used as the line centroid, and the resulting RB profile is normalized to the peak intensity. For RB_D, the line center of the primary component, which is derived from the RB_P-guided double Gaussian fit, is used as the line centroid and the resulting RB profile is normalized to the peak intensity of the primary component. As pointed out by Tian et al. (2011c), the RB_P technique can resolve the blueshifted secondary component more accurately as compared to the originally defined RB_S technique. Thus, here we apply the newly developed RB_P and RB_D techniques, as well as the RB_P-guided double Gaussian fit (for details see Tian et al. 2011c), to the data in this paper.

Figures 1–6 show the spatial distributions of the peak intensity, velocity, and exponential width derived from the SGF and the average RB_P asymmetry in the velocity interval of 70–130 km s^{-1} for Fe XIII λ202.04 or Fe XII λ195.12 in the observations of six events. For the RB_P asymmetry, a negative/positive value indicates an enhancement of the blue/red wing. We prefer to use the Fe XIII λ202.04 line to detect asymmetry since there is no identified blends in this strong line, although the pervasive presence of very weak redward asymmetries outside the dimming regions (in Figures 1–3) might suggest an unidentified weak blend at the red wing of the line profile. However, in Figures 4–6, we present results for the Fe XII λ195.12 line since the exposure time used in the associated observations is too short so that only the strong Fe XII λ195.12 line has enough S/N to allow a reliable RB asymmetry analysis

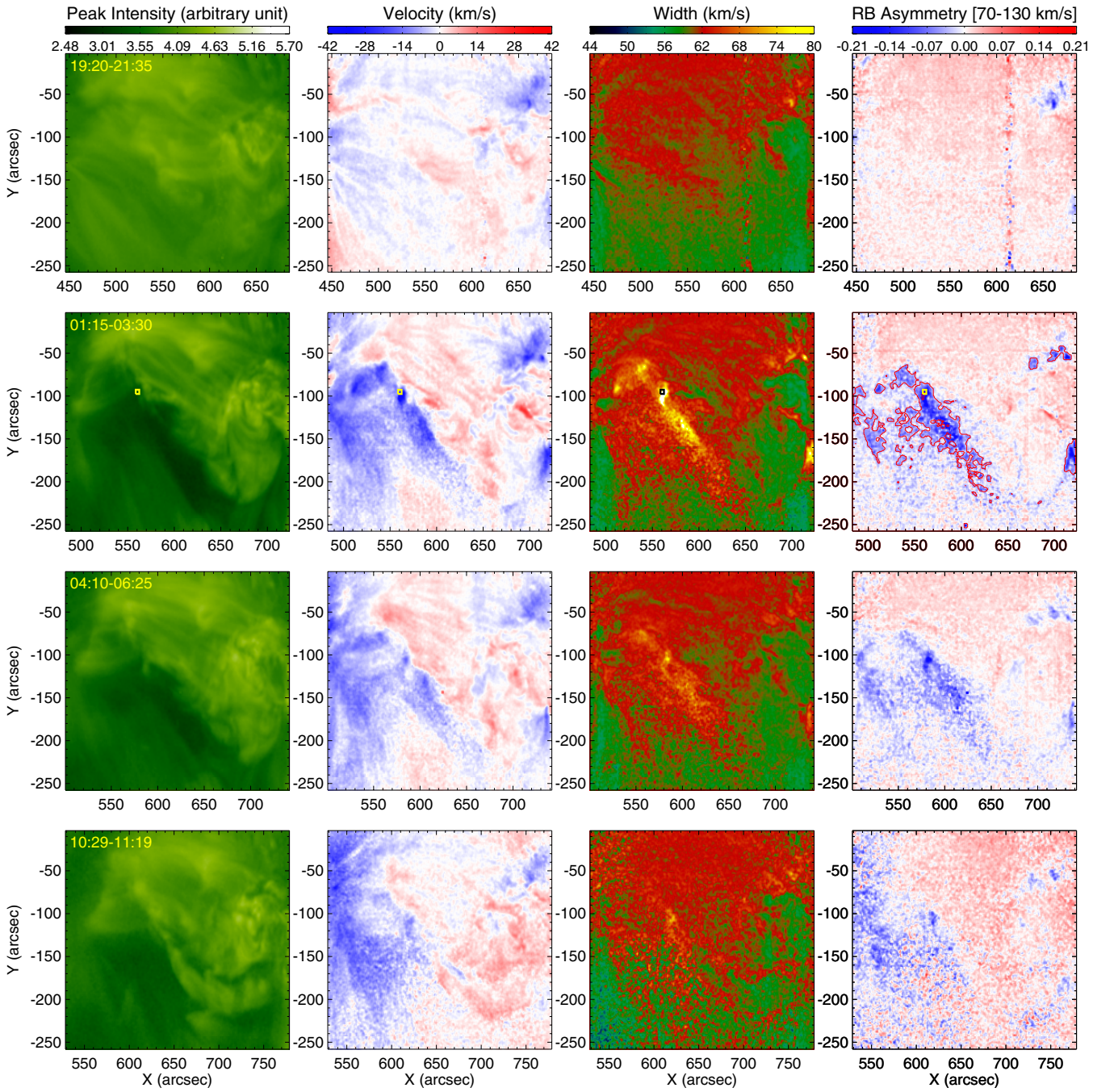

Figure 1. Spatial distributions of the peak intensity, Doppler velocity, and exponential width derived from the single Gaussian fit and the average RB_P asymmetry in the velocity interval of 70–130 km s^{-1} for Fe XIII λ202.04 in the 2006 December 14–15 observations. The beginning and ending time (hour:minute) of each scan is indicated in the intensity image. The pre-eruption conditions are shown in the first row. The square in each panel of the second row marks locations where profiles are averaged and presented in Figure 7. The red contours shown in the map of RB_P asymmetry for the 01:15–03:30 scan outline locations where the RB_P asymmetry (70–130 km s^{-1}) is smaller than −0.03 and the S/N of the profile is larger than 8.

(A color version of this figure is available in the online journal.)

for the individual profile. Since the blend Fe XII λ195.18 sits at the red wing of Fe XII λ195.12 (Young et al. 2009), any blueward asymmetries detected by our RB_P technique are not caused by this identified blend.

The pre-eruption parameters are presented in the first row of each figure. The scanned regions for all rasters are almost the same for almost every event. The only exception is the 2007 May 19 event shown in Figure 2, where we can clearly see that the observed region in the pre-eruption phase is about 50″ smaller in solar Y, compared to that in the eruption phase.

3. FLOWS

We found various types of flows in our observations. In the following, we mainly investigate properties of three types of outflows associated with the long-lasting coronal dimmings and the sudden CME or EUV jet eruptions.

3.1. Weak, High-speed Outflows in Dimming Regions

Coronal dimmings are clearly seen from the intensity images presented in Figures 1–4. The dimming regions are

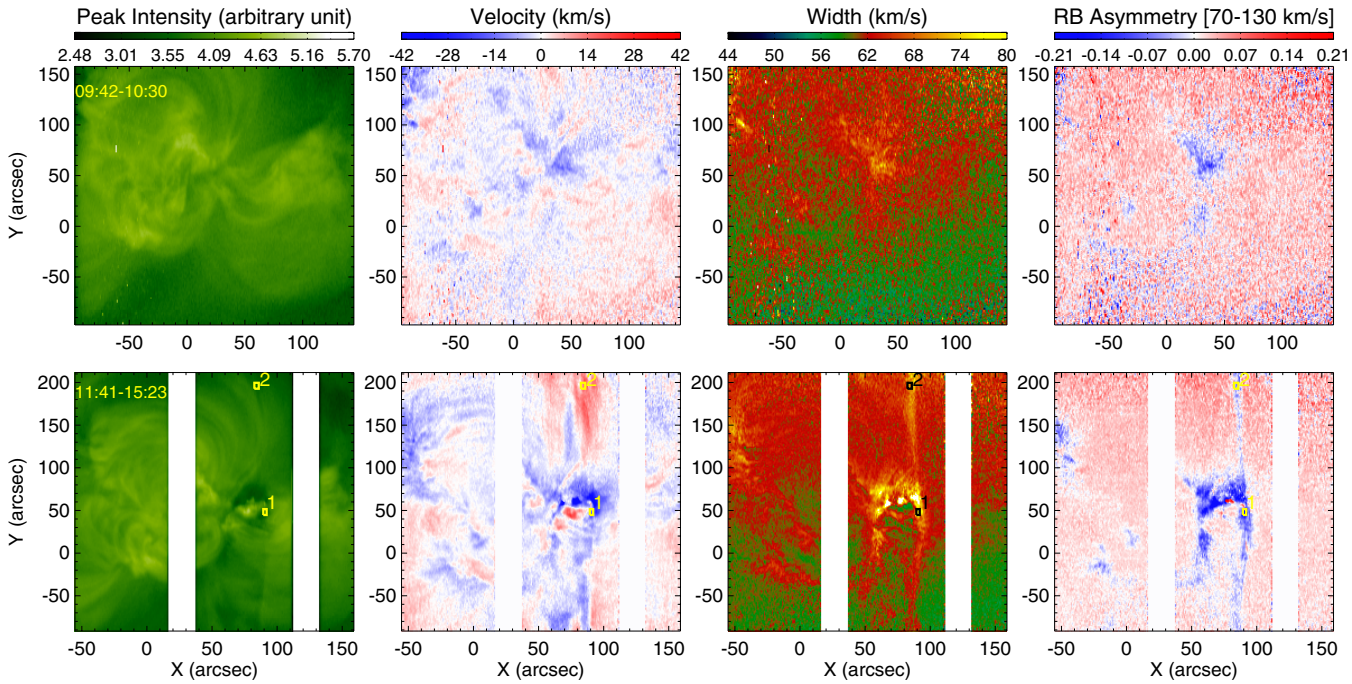

Figure 2. Same as Figure 1 but for the 2007 May 19 observations. The rectangular regions 1 and 2 mark the locations where the Fe XIII λ202.04 profiles are averaged and presented in Figure 8.

(A color version of this figure is available in the online journal.)

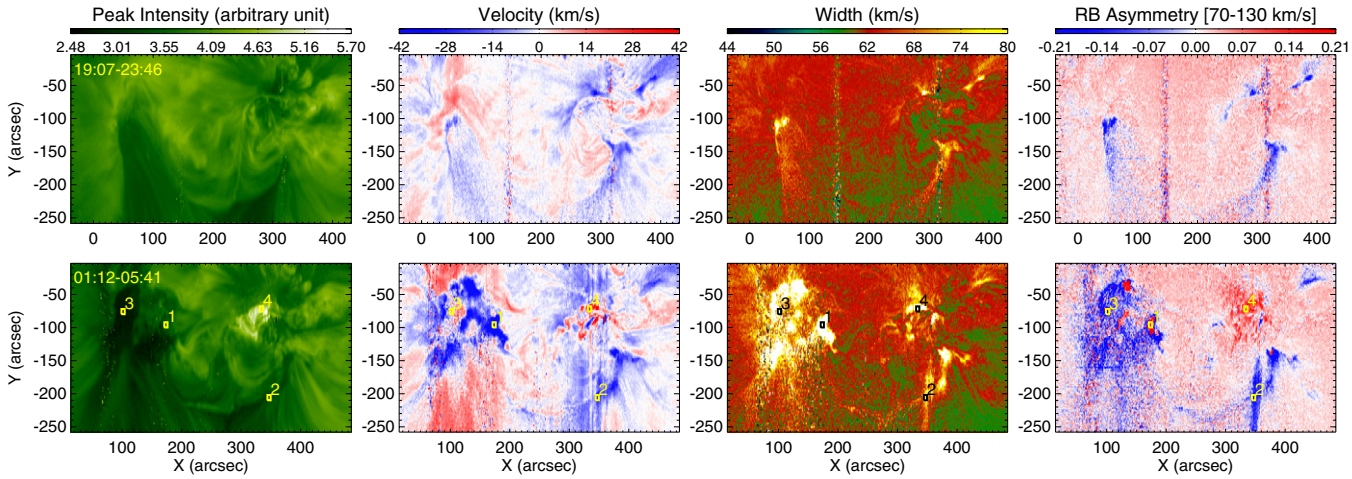

Figure 3. Same as Figure 1 but for the 2006 December 12–13 observations. The rectangular regions 1–4 mark the locations where line profiles are averaged and presented in Figures 10 and 14.

(A color version of this figure is available in the online journal.)

characterized by a blueshift of 10–40 km s^{-1}, a notable phenomenon in the *Hinode* era (Harra et al. 2007; Jin et al. 2009; Attrill et al. 2010; Chen et al. 2010; Harra et al. 2011a). Enhancement of the line width in dimming regions has also been reported by McIntosh (2009), Chen et al. (2010), and Dolla & Zhukov (2011), and it is very clear from Figures 1–4. The significant blueshift and enhanced line width are similar to those found at the weak-emission boundaries of ARs (e.g., Marsch et al. 2004, 2008; Harra et al. 2008; Del Zanna 2008; Del Zanna et al. 2011a; Doschek et al. 2007, 2008; Tripathi et al. 2009; He et al. 2010b; Murray et al. 2010; Brooks & Warren 2011; Warren et al. 2011; Bradshaw et al. 2011; Scott & Martens 2011; Young et al. 2012; Baker et al. 2012; Hara et al. 2008; De Pontieu et al. 2009; De Pontieu & McIntosh 2010; McIntosh & De Pontieu 2009a, 2009b; McIntosh et al. 2011; Peter 2010; Bryans et al. 2010; Ugarte-Urra & Warren 2011; Martínez-Sykora et al. 2011; Nishizuka & Harra 2011; Tian et al. 2011a, 2011c).

Figures 1–4 also reveal a significant blueward asymmetry in dimming regions. We note that the blueward asymmetries on maps of RB_S asymmetry for the 2006 December 14–15 observations, which were presented by McIntosh et al. (2010), are not as prominent as those in the RB_P asymmetry maps in our Figure 1. This is because of the underestimation of the degree of asymmetry by the RB_S technique (Tian et al. 2011c). The presence of obvious blueward asymmetries suggests that the line profiles in dimming regions probably contain a highly blueshifted secondary component besides the primary component. Such a scenario is similar to that of the chromospheric network and AR edges (e.g., Hara et al. 2008; De Pontieu et al.

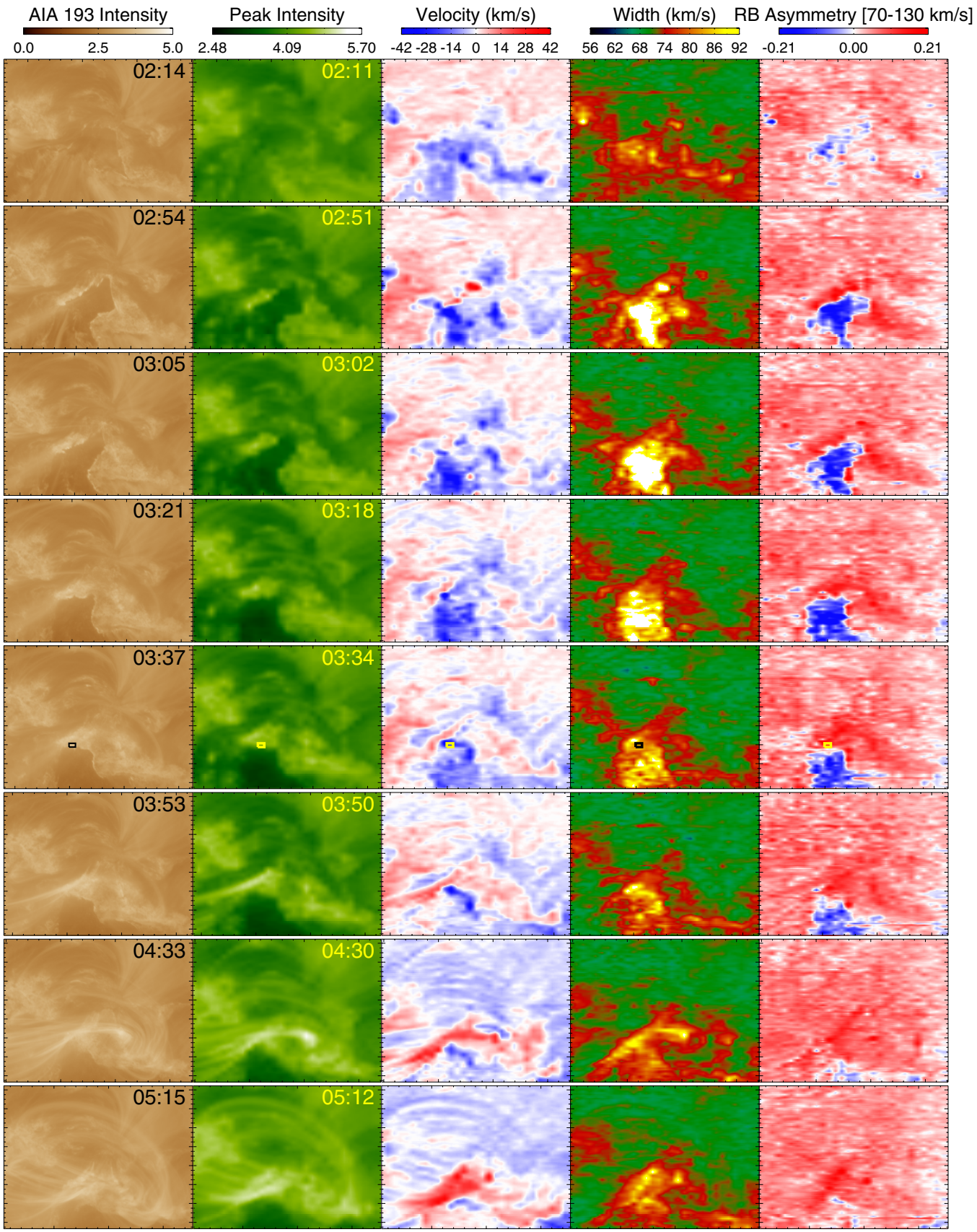

Figure 4. Evolution of AIA 193 Å intensity and EIS Fe XII λ195.12 line parameters (peak intensity, velocity, and width derived from the single Gaussian fit, and the average RB_P asymmetry in the velocity interval of 70–130 km s^{-1}) in the 2011 June 21 observations. The time of the AIA observation and the beginning time of each EIS scan are indicated in the corresponding intensity images. The rectangular region marks the locations where line profiles are averaged and presented in Figure 11. The size of the FOV is about 175″ × 152″. A movie (m4.mpeg) showing the evolution of AIA 171 Å is available online.

(An animation and a color version of this figure are available in the online journal.)

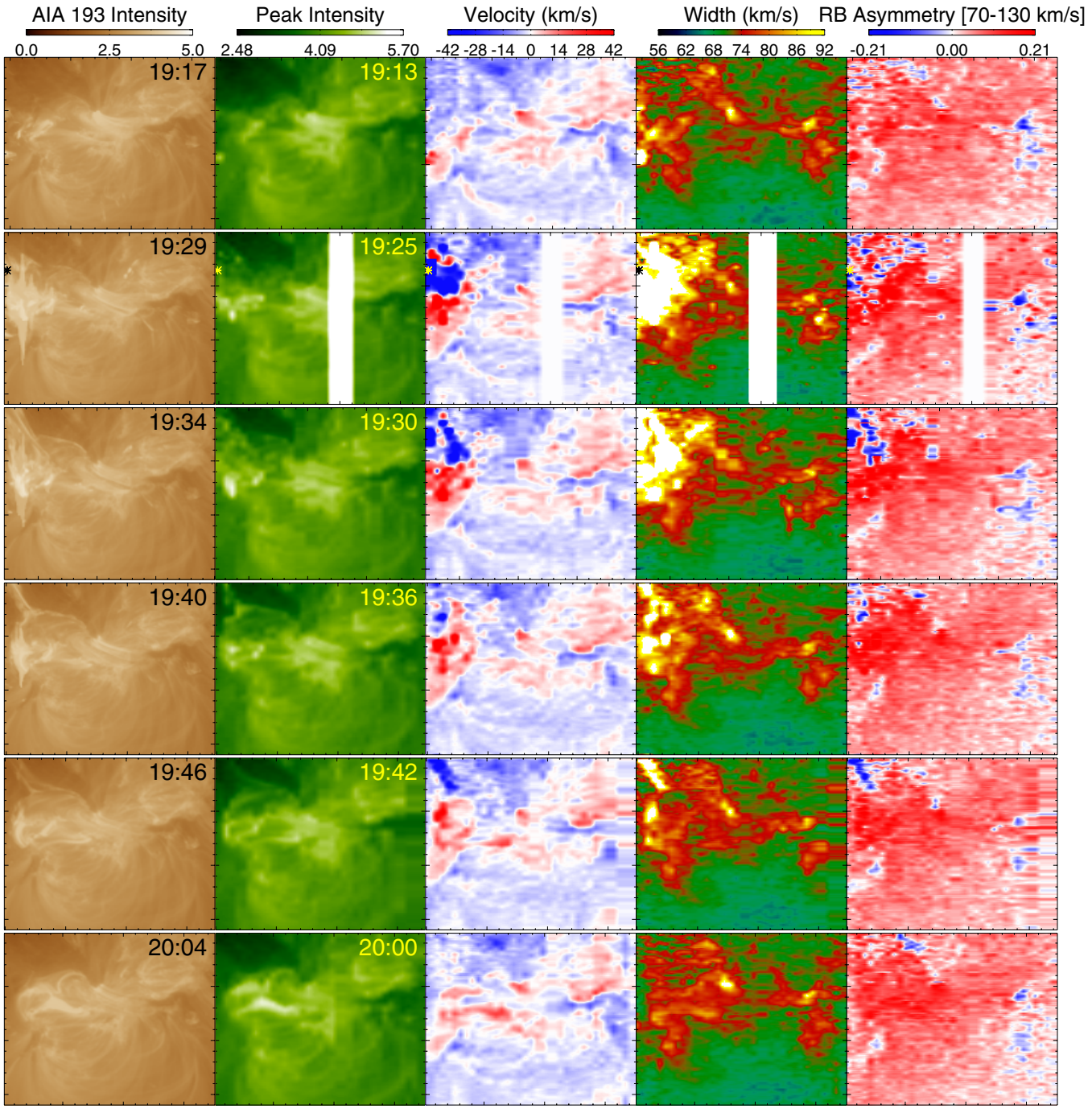

Figure 5. Same as Figure 4 but for the 2011 February 14 observations. The asterisk marks the center of five pixels along the slit where line profiles are averaged and presented in Figure 12. The size of the FOV is about $175'' \times 160''$. For illustration some bad data from single exposures are replaced by the data of adjacent exposures. A movie (m5.mpeg) showing the evolution of AIA 193 Å is available online.

(An animation and a color version of this figure are available in the online journal.)

2009; De Pontieu & McIntosh 2010; McIntosh & De Pontieu 2009a, 2009b; McIntosh et al. 2011; Peter 2010; Bryans et al. 2010; Tian et al. 2011a, 2011c; Ugarte-Urra & Warren 2011; Martínez-Sykora et al. 2011), and thus we can perform a similar analysis of the line profiles. For further analysis, we only selected those locations where the average RB_P asymmetry in the velocity range of 70–130 km s^{-1} is smaller than −0.03 (obvious blueward asymmetry) and the S/N of the profile (defined as the ratio of the peak and background intensities) is larger than 8. The RB_P-guided double Gaussian fit algorithm (see details in Tian et al. 2011c) was then applied to the profiles at these locations. After the double Gaussian fit, we took the spectral position of the primary component as the line centroid and calculated the RB_D asymmetry profile.

In Figures 7 and 8, we present several examples of the observed and fitted line profiles and the corresponding RB_P and RB_D asymmetry profiles in dimming regions. By comparing the observed profiles with the different fitting profiles, we can clearly see the better performance of the double Gaussian fits and the deviations of the observed profiles from the SGFs. The RB asymmetry profile is basically the difference between the emission of the two wings as a function of spectral distance

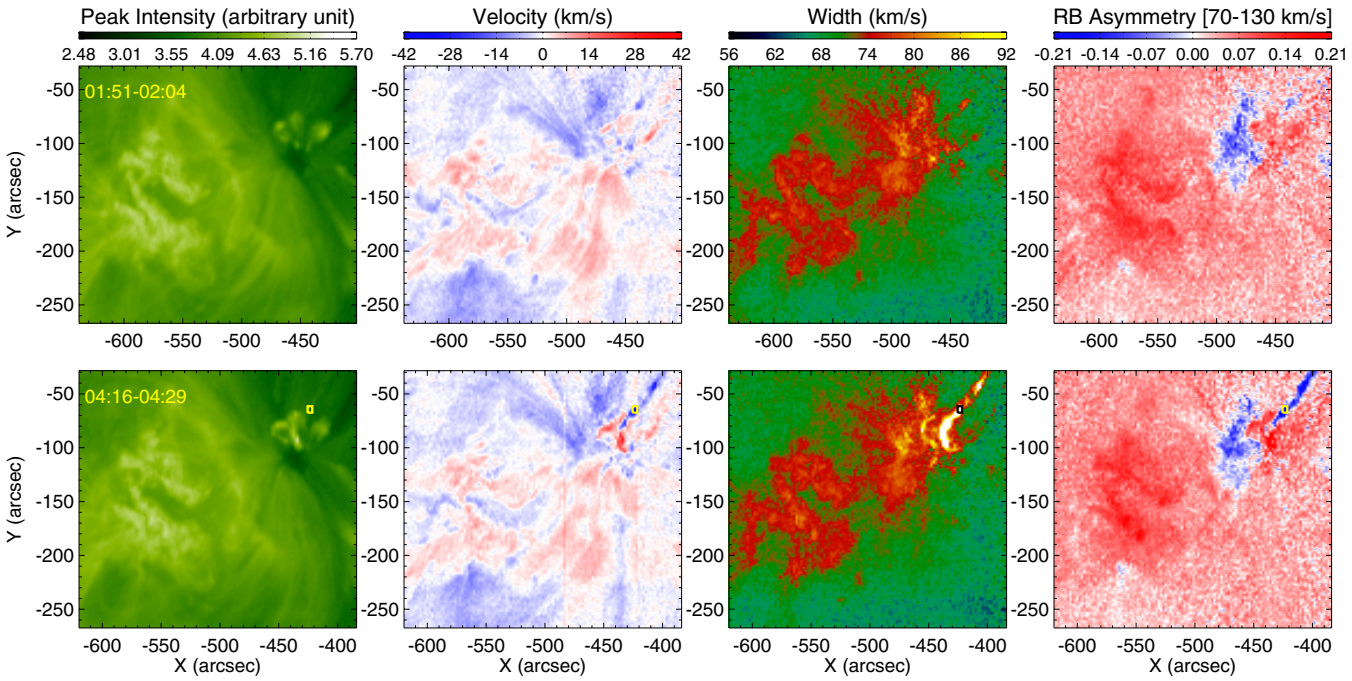

Figure 6. Same as Figure 1 but for Fe XII λ195.12 in the 2007 June 5 observations. The rectangular region marks the locations where line profiles are averaged and presented in Figure 13.

(A color version of this figure is available in the online journal.)

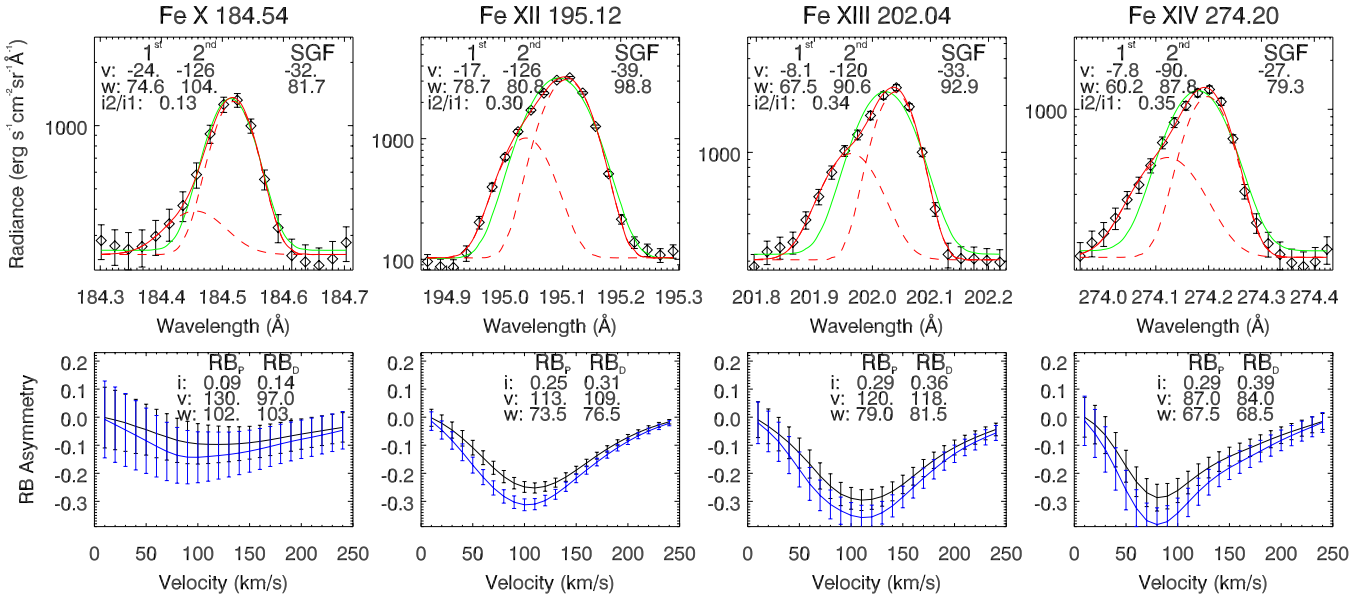

Figure 7. RB asymmetry profiles (bottom) of the Fe x λ184.54, Fe XII λ195.12, Fe XIII λ202.04, and Fe XIV λ274.20 line profiles (top) averaged over the square marked in Figure 1. Top: the observed spectra and measurement errors are shown as the diamonds and error bars, respectively. The green lines are single Gaussian fits. The two dashed red lines in each panel represent the two Gaussian components and the solid red line is the sum of the two components. The velocity (v) and exponential width (w) derived from the single (SGF) and double (1st/2nd for the two components) Gaussian fits are shown in each panel. Also shown is the intensity ratio of the secondary component to the primary one ($i2/i1$). Bottom: the black and blue lines represent RB profiles for RB_P and RB_D, respectively. Error bars indicate the errors propagated from the measurement errors. The peak relative intensity (i), velocity (v), and $1/e$ width (w) are shown in each panel.

(A color version of this figure is available in the online journal.)

(expressed in the velocity unit) from the line center. Here, a negative value means that the blue wing is enhanced with respect to the red wing at a certain spectral distance. The relative intensity and velocity of the secondary component can be derived from the peak of the RB asymmetry profile, and the $1/e$ width of the RB asymmetry profile is taken to approximate the width of the secondary component (see details in Tian et al. 2011c). As discussed in Tian et al. (2011c), the blend Si VII λ274.18 should not have an important influence on the results of our RB asymmetry analysis and double Gaussian fit for Fe XIV λ274.20 since the two lines are very close to each other and the maps of the Fe XIV λ274.20 line parameters resemble those of the clean Fe XIV λ264.78 line. Moreover, as mentioned in the following, the contribution of Si VII λ274.18 to the total emission is at most 5.4%. The Fe XII λ195.12 line is blended with Fe XII λ195.18, which sits at the red wing of

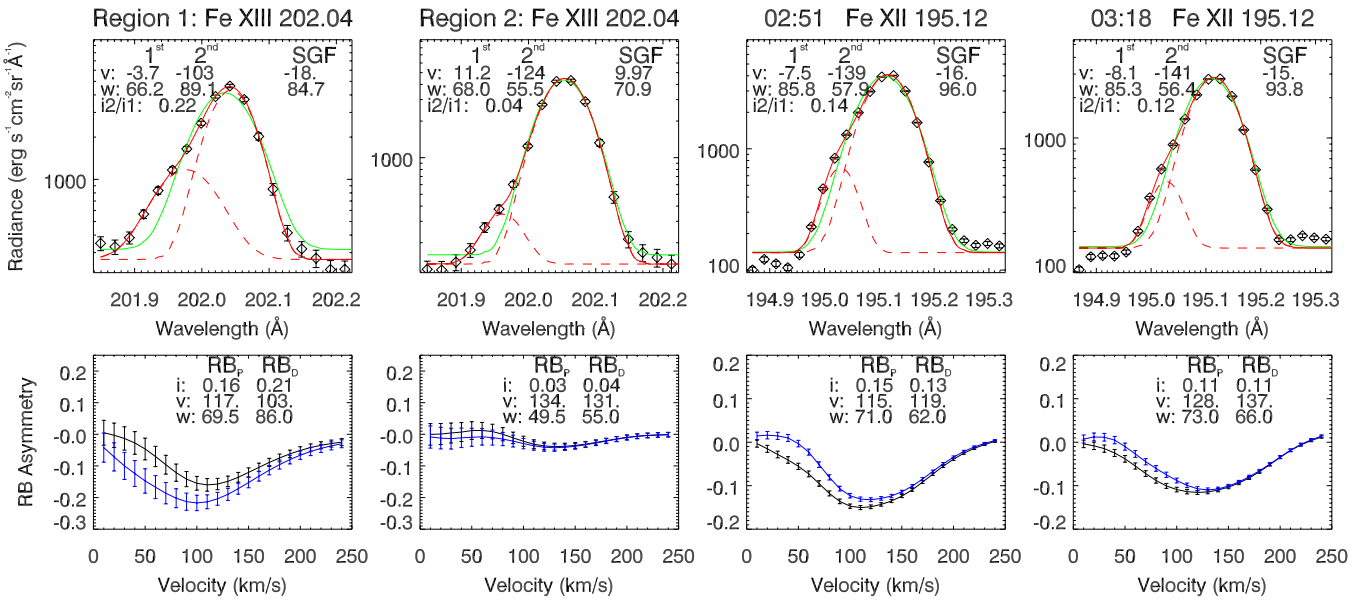

Figure 8. First and second columns: RB asymmetry profiles (bottom) of Fe XIII λ202.04 line profiles (top) averaged over regions 1 and 2 marked in Figure 2. Third and fourth columns: RB asymmetry profiles (bottom) of the averaged Fe XII λ195.12 line profiles (top) in dimming regions at 02:51 and 03:18 as shown in Figure 4. The line styles and denotations of parameters are the same as in Figure 7.

(A color version of this figure is available in the online journal.)

Fe XII λ195.12 so that any enhancement on the blue wing of the line profile is not caused by this identified blend. Thus, the blueward asymmetries of the Fe XII λ195.12 line profiles we observed here are real. The Fe X λ184.54 line is not as strong as the other three lines, and there is a weak Fe XI λ184.41 line at the blue side (Brown et al. 2008), making it difficult to derive the real degree of profile asymmetry. However, the Fe XI λ184.41 line is about 210 km s^{-1} away from the Fe X λ184.54 line and in normal conditions the two lines show up as two distinct peaks. So we believe that the enhancement between the two lines is due to the Fe X λ184.54 emission from a high-speed (∼100 km s^{-1}) outflow. As can be seen from Figure 7, we usually found that the blueward asymmetry is present at different coronal temperatures and that the velocity of the high-speed upflow does not show a dramatic change with temperature. However, we are aware that an accurate velocity determination is beyond the ability of the EIS instrument because of the large instrumental width and the complication by blends.

The ridge of enhanced line width for the 2007 May 19 11:41–15:23 scan, as shown in Figure 2, was previously reported by Chen et al. (2010). They found that this ridge corresponded to the outer edge of the dimming region. In the Dopplergram, blueshift of ∼10 km s^{-1} seems to be present in the southern part of the ridge (Chen et al. 2010), while the northern part shows net redshift, which seemed to be omitted by Chen et al. (2010). From the map of RB asymmetry, we can see that this ridge is also characterized by clear blueward asymmetry. Typical line profiles in both the southern and northern parts of the ridge are presented in Figure 8. Results of our RB asymmetry analysis indicate that the high-speed upflow is present along the whole ridge and that its speed might be ∼100 km s^{-1}.

We derived the parameters (relative intensity, velocity, and exponential width) of the high-speed secondary component by using the three methods (double Gaussian fit, RB_P, and RB_D), and in Figure 9 we present the histograms of these three parameters derived from Fe XIII λ202.04 line profiles in the 2006 December 15 01:15–03:30 observation (use profiles within the red contours shown in Figure 1). We can see that the relative intensity is usually around 10% and can sometimes reach more than 30%. The velocity is usually in the range of 50–150 km s^{-1}, and its distribution peaks around 90 km s^{-1}. The distribution of the exponential width peaks around 55 km s^{-1}, which is comparable to the width of the primary component. The distributions of the χ_r^2 for both the single and double Gaussian fits peak at values smaller than unity, which may result from the overestimation of the EIS measurement error (Peter 2010; Tian et al. 2011c). However, from the χ_r^2 ratio between the double and SGF we can see that the double Gaussian fit does better than the SGF for these asymmetric line profiles.

In Figure 9, we also show the relationship between the intensity/Doppler shift and the exponential width as derived from SGF, and the relationship between Doppler shift/exponential width derived from the SGF and the average RB_P asymmetry in the velocity interval of 70–130 km s^{-1}. There seems to be a weak anti-correlation between the SGF intensity and line width, which is consistent with the previous result that the intensity and line width show negative correlations in loop footpoint regions (Scott & Martens 2011) although the correlation turns into positive when considering the whole AR (Li & Ding 2009). Panel (F) reveals an obvious correlation between the SGF Doppler shift and line width. The calculated correlation coefficient is −0.59 if using all data points inside the red contours. Similar correlation was also found at AR boundaries (Doschek et al. 2007, 2008). As proposed by Doschek et al. (2008), this correlation may suggest that the profile is composed of multiple components. Indeed, we find striking correlations in panels (G) and (H) of Figure 9, with a correlation coefficient of 0.67 in (G) and −0.58 in (H). Such correlations strongly suggest that the clear blueshift and enhanced line width in dimming regions are largely caused by the blueward asymmetries. The growth of Alfvén wave amplitude, as suggested by McIntosh (2009), may be an additional reason for the enhancement of the line width. The fact may be that there is a faint high-speed upflow superimposed on a strong and almost stationary (or slightly shifted)

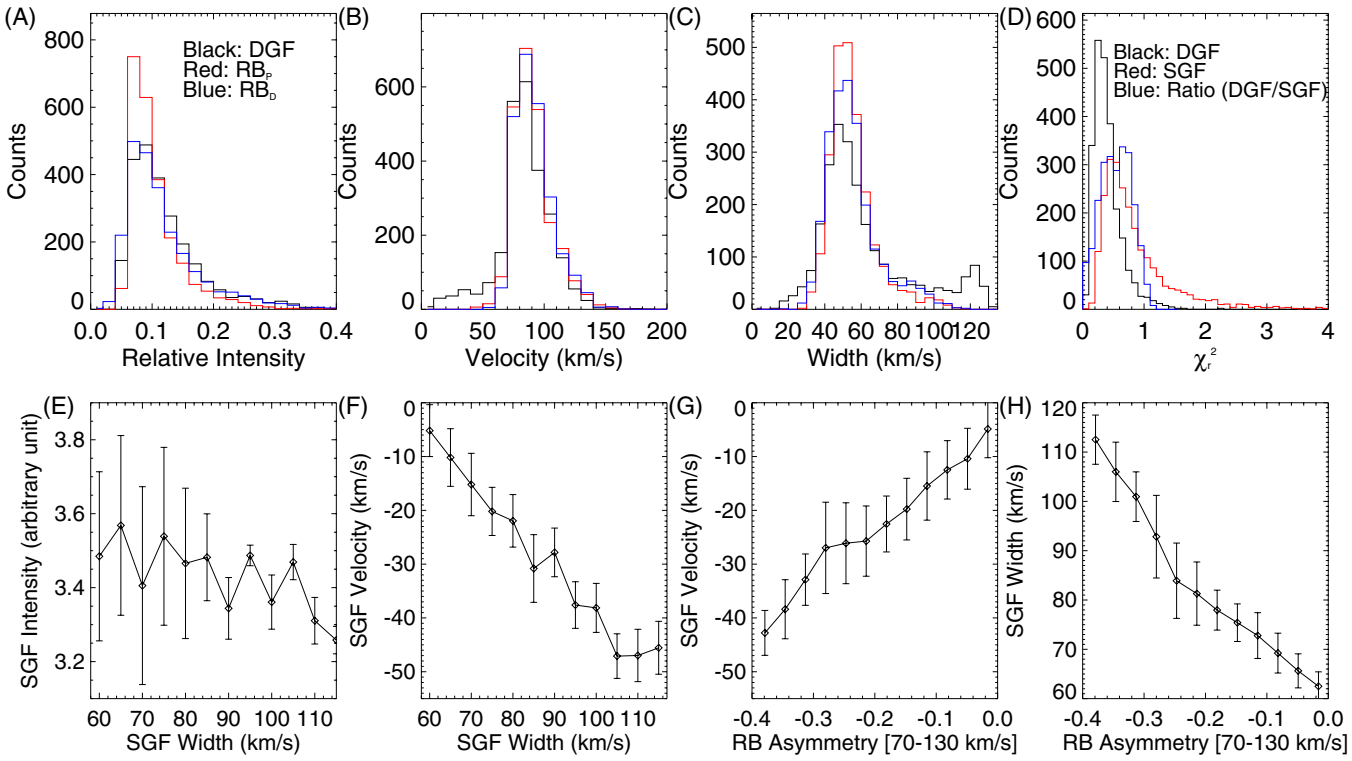

Figure 9. Histograms of the relative intensity (A), velocity (B), and exponential width (C) of the secondary component, as derived from double Gaussian fit (black) and RB asymmetry analysis (red/blue for RB_P/RB_D) for Fe XIII λ202.04 in the 2006 December 15 01:15–03:30 observation. Panel (D) shows the histograms of the χ_r^2 values of the single (red) and double (black) Gaussian fits, as well as the ratio of the two (blue). Panels (E) and (F) show the relationship between the intensity/Doppler shift and the exponential width as derived from single Gaussian fit. Panels (G) and (H) present the relationship between the Doppler shift/exponential width derived from single Gaussian fit and the average RB_P asymmetry in the velocity interval of 70–130 km s^{-1}.

(A color version of this figure is available in the online journal.)

background in the LOS direction. This scenario is also similar to the inhomogeneities of flow velocities along the LOS as proposed by Dolla & Zhukov (2011) and would naturally produce blueward asymmetric line profiles. An SGF to the total emission line profile would yield a blueshift and enhanced line width, as compared to the line profile of the background emission. When the relative intensity of the high-speed upflow component becomes larger, the blueward asymmetry becomes more obvious and we will obtain a larger blueshift and line width if applying an SGF. The intrinsic assumption of an SGF is that everything is moving at the same bulk speed, which is obviously not the case in coronal dimming regions. Thus, our analysis implies that previous results based on an SGF cannot reflect the real physical processes and thus may need to be reconsidered. First, the outflow speed in dimming regions is perhaps not around 20 km s^{-1}(Harra et al. 2007; Jin et al. 2009; Attrill et al. 2010; Chen et al. 2010; Harra et al. 2011a) but can easily reach ∼100 km s^{-1} in the lower corona. Such a velocity difference is important since different velocities might be associated with different physical processes. Second, the enhanced line width is not purely due to the increase of the Alfvén wave amplitude (McIntosh 2009) but is largely contributed by the superposition of different emission components.

We note that the properties of these high-speed outflows are very similar to those we found previously in AR edges (Tian et al. 2011c). This similarity suggests that the outflows in both regions may result from a similar process, e.g., heating in the lower atmosphere (De Pontieu et al. 2009; McIntosh & De Pontieu 2009b; Hansteen et al. 2010; Song & Vasyliūnas 2011). Magnetohydrodynamic simulations have shown that magnetic reconnection is an efficient mechanism to produce high-speed outflows (jets) in the lower solar atmosphere (e.g., Ding et al. 2011; Roussev et al. 2001). As the magnetic field lines opened up by CMEs, rapid multi-thermal upflows produced by both the pre-existing and CME-induced impulsive heating at the lower part of the erupted loops are guided by the field lines into the transiently opened corona. These outflows may serve as an important source of materials to refill the corona. From Figures 1 and 4 we can see that the blueward asymmetries were strongest within a few hours after the flare peak time, indicating that the high-speed outflows were strongest right after the erupted materials left the Sun. As the dimmings gradually recovered and the magnetic fields began to close down again, the outflows became weaker. Such a result is consistent with the finding of Miklenic et al. (2011) that the mass loss occurs mainly during the period of strongest CME acceleration.

Through joint imaging and spectroscopic observations of the corona, McIntosh & De Pontieu (2009a), De Pontieu & McIntosh (2010), and Tian et al. (2011a, 2011c) have suggested that the secondary emission component found at AR edges is caused by high-speed repetitive upflows in the form of upward propagating disturbances (PDs) in EUV and X-ray imaging observations. Similarly, we think that the highly blueshifted component found in spectra of dimming regions should exhibit as PDs in imaging observations. The *SDO*/AIA observations, with a high S/N (especially in the 171 Å and 193 Å passbands) and high cadence, might be able to reveal such weak PDs. The 2011 June 21 observations were done in the *SDO* era, and from the associated movie (m4.mpeg) of Figure 4 we can clearly see the evolution of the dimming boundary, which is likely to

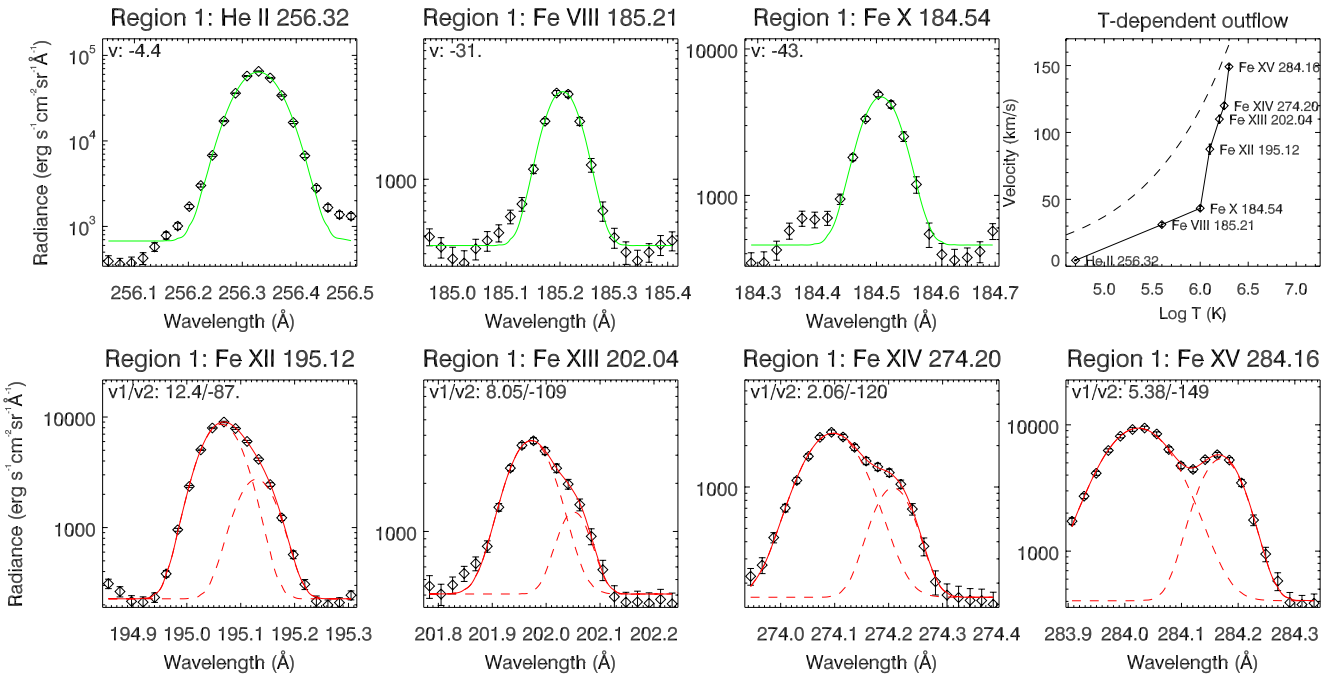

Figure 10. Line profiles averaged over region 1 marked in Figure 3. The diamonds, error bars, line styles, and colors are the same as in Figure 7. The velocities (v) derived from the single (SGF) and double ($v1$ and $v2$ for the two components) Gaussian fits are shown in each panel. Also shown is the temperature-dependent outflow velocity and the adiabatic sound speed (dashed curve in the upper right panel).

(A color version of this figure is available in the online journal.)

be associated with the successive disappearance of the "moss" (McIntosh et al. 2007). In addition, there seems to be weak outward PDs along legs of the opened coronal loops. However, both the LOS effect and the significantly reduced emission associated with these opened field lines make it difficult to study the PDs quantitatively. Part of these outflows may experience further acceleration at higher layers, overcome the gravity, and eventually become the solar wind stream along the transiently opened field lines, which may serve as an additional momentum source for the associated CME (McIntosh et al. 2010). They might provide additional acceleration or dragging of the CME. We also noticed that the ascending post-flare loops revealed by the movie were clearly observed by EIS (last row of Figure 4), showing a blueshift of $\sim$5 km s^{-1}. Ascending pre-flare loops were reported by Harrison & Bewsher (2007).

3.2. Temperature-dependent Outflows at the Edges of Dimming Regions

A temperature-dependent outflow was reported by Imada et al. (2007), who found that the flow speed increases from $\sim$10 km s^{-1} at log (T/K) = 4.9 to $\sim$150 km s^{-1} at log (T/K) = 6.3 in a dimming region. However, we found that this temperature-dependent outflow is not in but immediately outside the deepest (darkest in the intensity image) dimming region. More interestingly, we found that our RB$_P$ technique can identify this temperature-dependent outflow. This event was located around ($x = 135''$, $y = -35''$) in Figure 3, and we can see that it is associated with a small patch of redward asymmetry. This is easy to understand since the outflow component is much stronger than the background emission component in Fe XIII λ202.04, as can be seen from Figure 3(f) of Imada et al. (2007).

We further identified several temperature-dependent outflows in the 2006 December 13 01:12–05:41 observation. These temperature-dependent outflows are associated with the small patch of redward asymmetry around the location of ($x = 130''$, $y = -85''$), ($x = 175''$, $y = -95''$), ($x = 375''$, $y = -135''$), and ($x = 135''$, $y = -35''$), respectively. All of these temperature-dependent outflows are not in but immediately outside the deepest dimming region. As an example, Figure 10 shows the line profiles of the temperature-dependent outflow around ($x = 175''$, $y = -95''$), region 1 in Figure 3. An SGF seems to be adequate to derive the outflow velocities for the emission lines formed at a temperature of log (T/K) $\leqslant$ 6.0. For emission lines formed at higher temperatures, we see clear indications of two well-separated components in the line profiles. Thus, we applied a double Gaussian fit to these line profiles, and the Doppler shift of the highly blueshifted component (denoted as $v2$ in Figure 10) should represent the outflow velocity at the corresponding temperature. The small-velocity component, whose velocity is denoted as $v1$, is likely to be the nearly stationary background emission of the corresponding ion. Since we are mainly interested in the velocity of the highly blueshifted component and this component is often stronger than the background component, the outflow velocity derived from the double Gaussian fit should be highly reliable. We can see that the temperature variation of the outflow velocity shown in Figure 10 is similar to Figure 6 of Imada et al. (2007).

We also identified temperature-dependent outflows in the 2011 June 21 observation. Unfortunately, the exposure time used in this observation is only 9 s so that only the Fe XII λ195.12 line can be used for asymmetry analysis without any temporal or spatial binning. From Figure 4, we can see enhanced redward asymmetries surrounding the region of significant blueward asymmetry (dimming region). The blend of Fe XII λ195.18 certainly contributes to these redward asymmetries. However, if we spatially bin line profiles of various lines at several adjacent pixels there, we start to see clear signatures of temperature-dependent outflows. Thus, both the blend of Fe XII λ195.18 and the temperature-dependent outflows are causing these redward

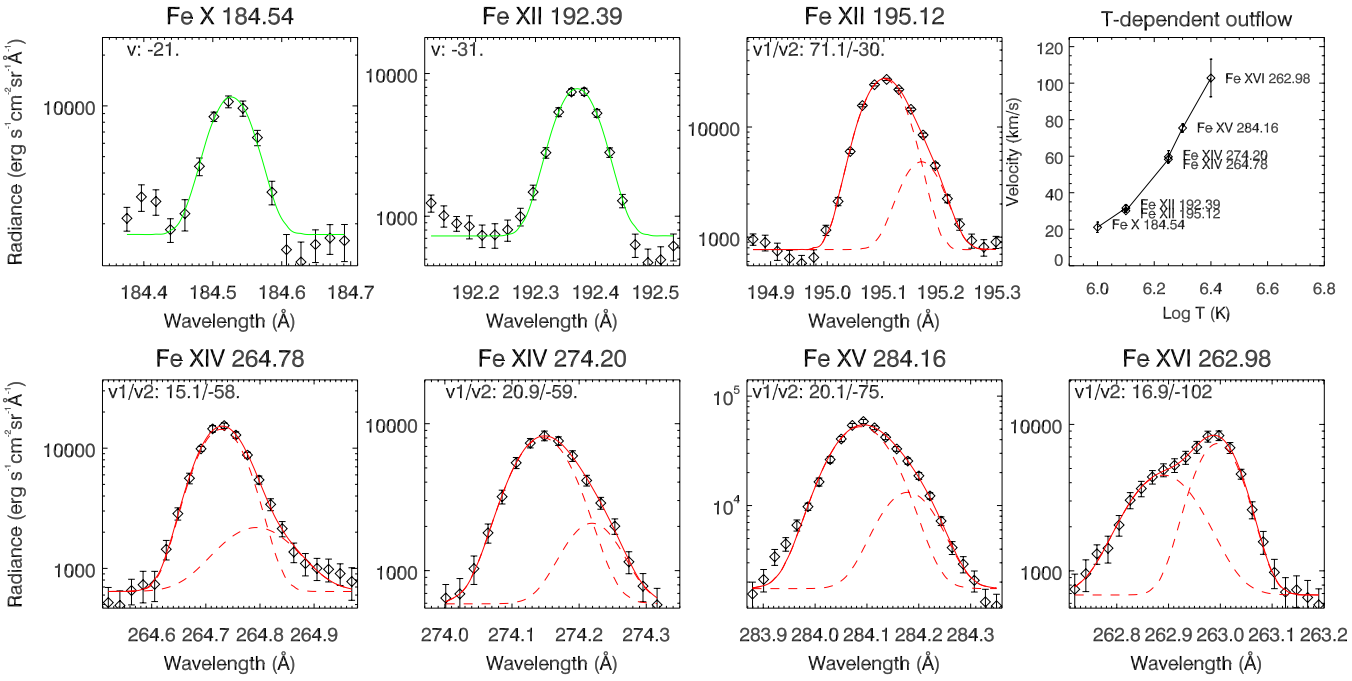

Figure 11. Same as Figure 10 but for the rectangular region marked in Figure 4.
(A color version of this figure is available in the online journal.)

asymmetries. As an example, we present in Figure 11 the line profiles averaged over the small rectangular region marked in Figure 4. Similar to Figure 10, single or double Gaussian fits are applied to these line profiles to obtain the outflow velocities at different temperatures.

From Figures 3 and 4, we can also see the enhancement of the line width at locations where the temperature-dependent outflows are found. These enhanced line widths, as derived from SGFs, are actually caused at least partly by the superposition of the relatively weak background emission component and the strong outflow component for Fe XIII λ202.04 and Fe XII λ195.12, as demonstrated in Figures 10 and 11, respectively.

Note that there are several blends of the He II λ256.32 line. However, the He II λ256.32 line usually dominates and contributes more than 80% of the total emission in disk observations (Young et al. 2007). The Fe VIII λ185.21 is blended with Ni XVI λ185.23, but the blend should not have a large impact on the derived velocity, since the two lines are very close to each other and the latter is much weaker than the former (Young et al. 2007). The enhancement of the blue wing in the Fe XV λ284.16 line profile, at around 283.95 Å in Figure 11, seems to be caused by the weak blend Al IX λ284.03 (Young et al. 2007) and should not impact the derived velocity of the very strong outflow component significantly.

The fact that these temperature-dependent outflows are found outside the (deepest) dimming regions suggests that these outflows are different from the high-speed outflows we described in the previous section. The temperature-dependent nature of these outflows resembles that of gentle (as opposed to explosive) chromospheric evaporation flows. Gentle chromospheric evaporation can be driven by low-flux ($\leqslant 10^{10}$ ergs cm^{-2} s^{-1}) nonthermal electron beams in the flare impulsive phase (e.g., Milligan et al. 2006b) or thermal conduction in the flare decay phase (e.g., Antiochos et al. 1978; Berlicki et al. 2005). The temperature-dependent outflows we present here are away from the flare sites so that they may not be directly related to the associated flares at first thought. However, we cannot exclude the possibility that some magnetic field lines there are connected to the flare sites and that nonthermal electron beams or enhanced thermal conduction resulting from the flares cause the evaporation flows. For the 2006 December 12–13 event we may exclude the possibility of nonthermal electron beams since most temperature-dependent outflows were identified after the flare peak time. It is also possible that interactions between the opened field lines in the dimming region and the closed loops in the surrounding plage region produce low-flux nonthermal electrons or/and enhanced thermal conduction, which will then generate the evaporation flows.

The difference between the high-speed outflows in dimming regions and the temperature-dependent outflows immediately outside the (deepest) dimming regions can also be understood in the sense of driving force. The former are perhaps driven by magnetic reconnection in the chromosphere or TR. These multi-thermal outflows usually do not show obvious temperature dependence since the acceleration by magnetic force finishes at locations very close to the reconnection site (e.g., Yokoyama & Shibata 1995). As discussed above, the latter seem to be evaporation flows that are driven by pressure gradient force. Thus, the acceleration will continue as long as a pressure gradient exists (e.g., Kamio et al. 2009; Shimojo et al. 2001; Judge et al. 2012). The dramatic increase of the flow speed from $\log(T/\mathrm{K}) \leqslant 6.0$ to $\log(T/\mathrm{K}) \geqslant 6.0$, as shown in Figure 10, is similar to that of the event analyzed by Imada et al. (2007) and may be caused by a steep pressure (temperature) gradient at a certain height (Imada et al. 2011).

3.3. Strong, Highly Blueshifted Component Representing the Ejecta Emission

No pronounced dimming was recorded by EIS for the 2011 February 14 and 2007 June 5 observations. However, clear

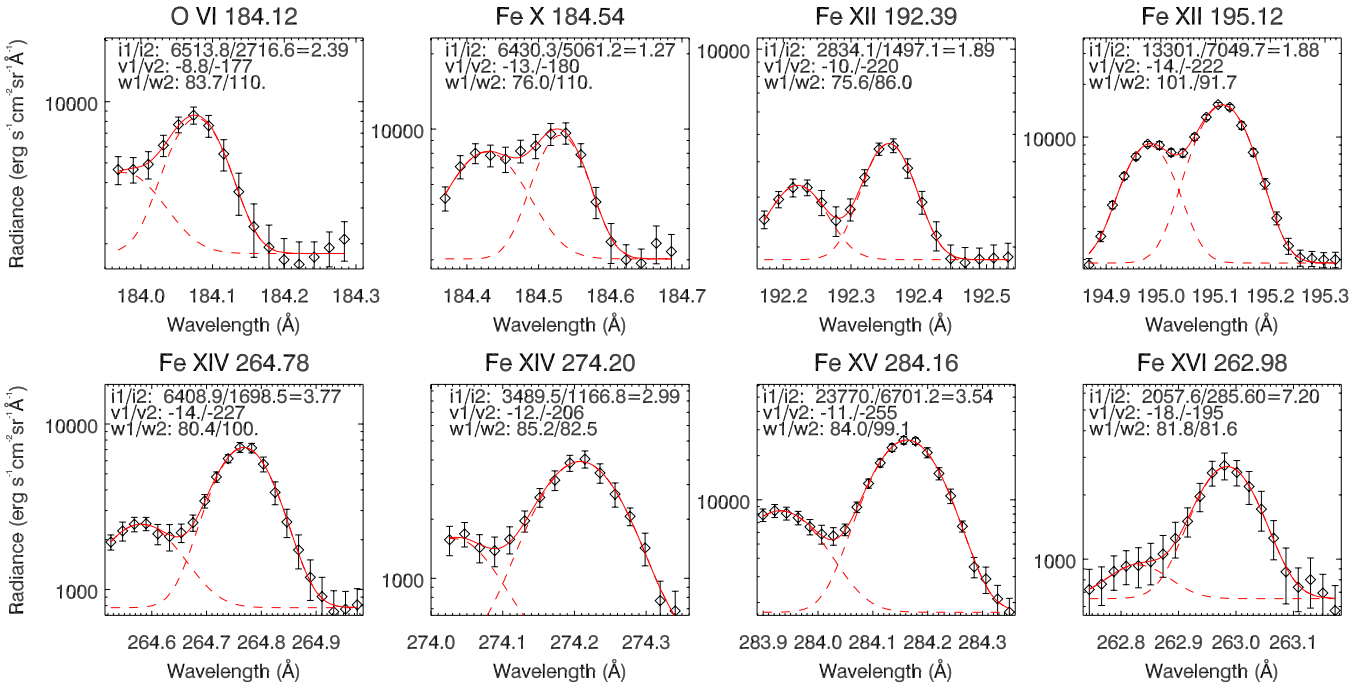

Figure 12. Line profiles averaged in locations marked in Figure 5. The diamonds, error bars, line styles, and colors are the same as in Figure 7. The peak intensities ($i1$ and $i2$), velocities ($v1$ and $v2$), and exponential widths ($w1$ and $w2$) of the two Gaussian components are shown in each panel.

(A color version of this figure is available in the online journal.)

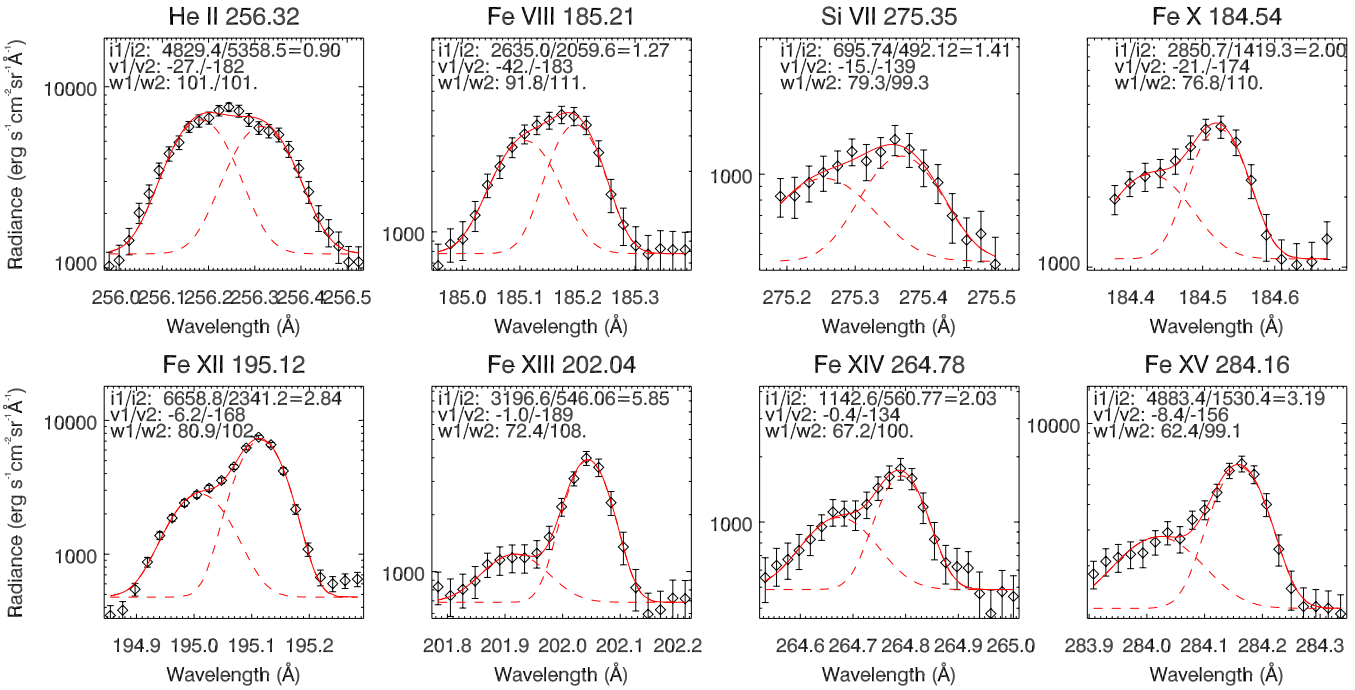

Figure 13. Same as Figure 12 but for the rectangular region marked in Figure 6.

(A color version of this figure is available in the online journal.)

plasma ejections (CME or EUV jet) were observed, and the associated line profiles clearly exhibit two well-separated components. The eruption of the CME loop on 2011 February 14 was clearly revealed in the AIA 304 Å, 171 Å, and 193 Å passbands; (see m5.mpeg showing the evolution of the 193 Å passband, the green box indicates the FOV of the EIS observation). For imaging observations of the 2007 June 5 jet, we refer to Yang et al. (2011). Figures 12 and 13 show an example of line profiles associated with the CME ejecta and the EUV jet, respectively. It is clear that emission lines formed at coronal and TR temperatures clearly exhibit two well-separated components, an almost stationary component accounting for the background emission and a highly blueshifted component representing emission from the erupting material. The Doppler velocities of the two components can be easily calculated through a double Gaussian fit.

From Figure 12, we can see that the highly blueshifted component has a velocity of ∼220 km s^{-1} and the velocity does not change significantly with temperature. This velocity should represent the LOS velocity of the CME ejecta (expanded loops) at 19:29 on 2011 February 14. The POS component of the ejecta velocity was estimated to be ∼200 km s^{-1} from simultaneous AIA 193 Å observations. Combining the two velocity components, we can calculate the real speed of the ejecta at 19:29, which is ∼300 km s^{-1}. Unfortunately, the fast EIS scans only focused on the same region so that the oblique propagation of the CME ejecta was not fully tracked. But in principle one should be able to track the complete evolution (not only the POS component) of CMEs by using simultaneous imaging and spectroscopic observations. We noticed that clear line splittings interpreted as filament or plasmoid eruptions at similar speeds were previously reported by Harra & Sterling (2003) and Asai et al. (2008).

From Figure 13 we can see that the blueshifted component, which is apparently associated with the EUV jet, has a speed of ∼170 km s^{-1}. The fact that we do not see an obvious temperature dependence of the flow speed suggests that this EUV jet is produced by reconnection instead of evaporation (Kamio et al. 2009). Since the POS component of the jet speed is ∼145 km s^{-1} (Yang et al. 2011), the real speed is calculated to be ∼223 km s^{-1}. From Figure 13, we can also see that the intensity ratio of the nearly stationary component and the highly blueshifted component ($i1/i2$) increases from 0.90 at log (T/K) = 4.7 to 5.85 at log (T/K) = 6.2. Such an increase should be directly related to the difference in the temperature distribution (differential emission measure, DEM, discussed below) of the background emission and the jet emission. It is likely that the decrease of blueshift with temperature, as derived by Yang et al. (2011) from an SGF, is in fact caused by this increase of intensity ratio and thus cannot reflect the real physical process. In addition, the very large nonthermal velocities (∼100–400 km s^{-1}) reported by Kim et al. (2007) and Yang et al. (2011) through SGFs are also likely to be caused by the effect of the superposition of the two (background and jet) emission components.

Another feature that is worth noting is the inverted Y-shape structure at one footpoint of the erupted loop (the fifth row of Figure 5) and the base of the jet (the second row of Figure 6). A net redshift and enhanced line width are found at the base of the inverted Y-shape structure in each case. Redshifts have been previously reported at the base of a polar jet and an AR jet by Kamio et al. (2007) and Chifor et al. (2008b), respectively. It is likely that they are caused by the downward propagating reconnection outflows, which collide with and compress the underlying loops (Yokoyama & Shibata 1995). And the enhanced line widths perhaps result at least partly from the flow inhomogeneities in this process. It seems that significant redward asymmetries are also found at the bases of the inverted Y-shape structures, but they are complicated by the blend Fe XII λ195.18. However, by averaging profiles of some weaker but clean lines over several spatial pixels at the bases of the inverted Y-shape structures, we do see signatures of redward asymmetries (not shown here), which may be caused by the downward flows.

At the end of this section, we would like to discuss various types of flows found in the 2006 December 12–13 observations. For detailed descriptions of this event, we refer to Kubo et al. (2007), Zhang et al. (2007), Asai et al. (2008), Jing et al. (2008), and Fan (2011). From Figure 3, we can see that before eruption (19:07–23:46) the loop footpoint regions are characterized by clear blueshift, enhanced line width, and obvious blueward asymmetry. Such results indicate the presence of a weak, high-speed upflow superimposed on the nearly stationary background (e.g., De Pontieu et al. 2009; McIntosh & De Pontieu 2009a; Tian et al. 2011a, 2011c; Martínez-Sykora et al. 2011). During eruption (01:12–05:41) there was a clear expansion of the regions with clear blueshift, enhanced line width, and obvious blueward asymmetry. Line profiles in the newly formed dimming regions (e.g., profile of region 3 shown in Figure 14) are obviously blueward asymmetric and thus are similar to those of loop footpoint regions, indicating the presence of rapid upflows along the opened field lines as discussed in Section 3.1. The elongated blueward-asymmetry feature was observed in the flare impulsive phase and was not located in the dimming region. The line profiles there (e.g., profile of region 2 shown in Figure 14) clearly reveal two components, and the high-speed component is likely to be associated with the initial removal of the magnetic loop. From Figure 3 we can also see patches of significant redward asymmetries around the flare site (around $x = 330''$, $y = -80''$). Figure 14 shows profiles of two lines in a small region (region 4 marked in Figure 3), and the redward asymmetries are clearly revealed in both the SGFs and RB_P asymmetry profiles. Such asymmetries clearly indicate that the enhanced nonthermal broadening is caused by the superposition of flows, i.e., turbulence (Milligan 2011). We found a net redshift of ∼30 km s^{-1} for almost all strong lines used in this observation. This multi-thermal downward motion is perhaps driven by both the cooling of the flare plasma and the overpressure of the flare plasma relative to the underlying atmosphere.

4. PLASMA DIAGNOSTICS

4.1. Dimmings

Using CDS data, Harrison & Lyons (2000) and Harrison et al. (2003) made first efforts to diagnose the electron densities and calculate the mass losses of dimming regions observed at the limb. They concluded that the reduced emission in dimming regions is an effect of mass loss rather than temperature change. They also mentioned the importance of calculating mass losses of on-disk dimming regions in the context of space weather forecast. Based on static solar atmosphere models, Jin et al. (2009) also tried to calculate the mass losses of two dimming regions by using EIS observations.

Here, we extend these previous investigations and make efforts to diagnose the electron density, temperature, and mass loss for the dimming regions we study in this paper. By comparing the intensity images of various emission lines before (19:20–21:35) and after (01:15–03:30) the eruption for the 2006 December 14–15 event (Figure 15), we can clearly see the occurrence of dimming at all temperatures. We then averaged line profiles over the regions where the intensity was reduced more than 20% and calculated intensities of different lines before and after the eruption. By using the routine *chianti_dem.pro* (also used by Lee et al. 2011) available in SolarSoft and assuming a constant pressure of 10^{16} cm^{-3} K, we obtained the DEM curves at the pre-eruption phase and of the dimming region. Here, a double Gaussian fit was applied to the Fe XI λ188.23 line profiles to derive the input line intensities since Fe XI λ188.23 is partly blended with the strong Fe XI λ188.30 line (Young et al. 2007), while we applied SGFs to

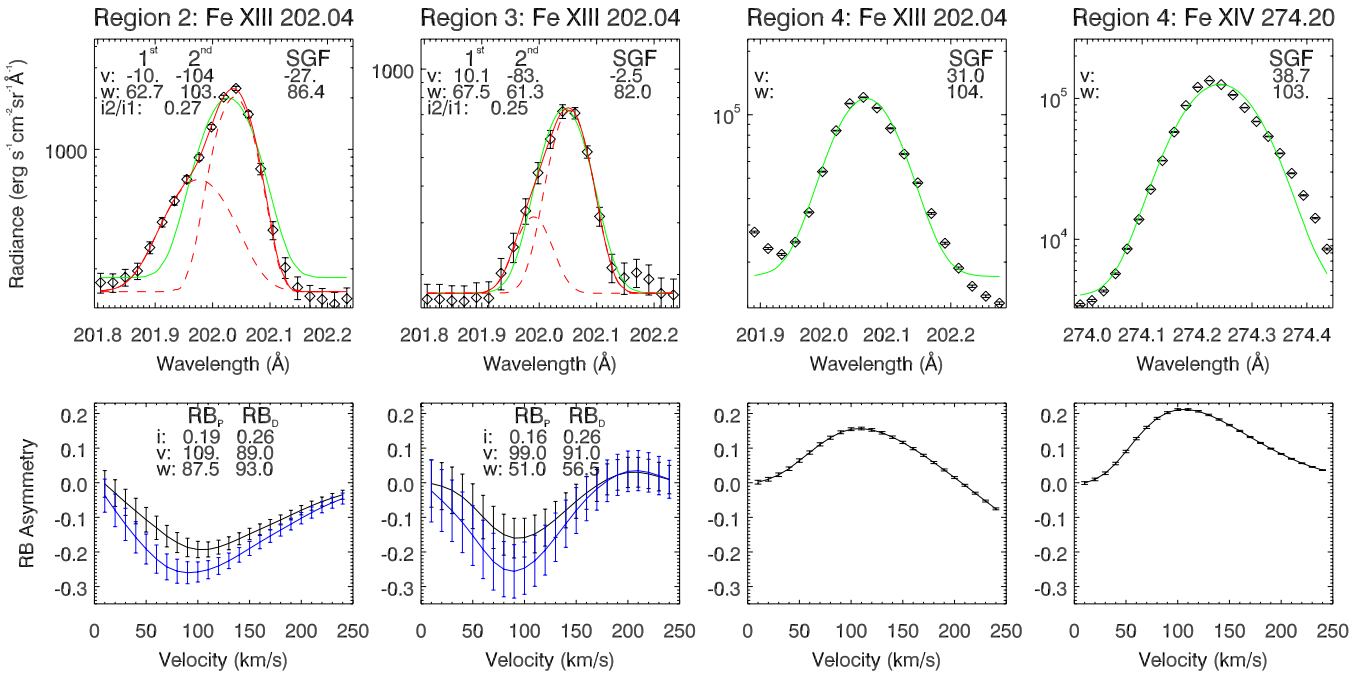

Figure 14. Similar to Figure 7 but for regions 2–4 marked in Figure 3. For the averaged profiles in region 4 only the single Gaussian fits and the RB$_P$ asymmetry profiles are plotted.

(A color version of this figure is available in the online journal.)

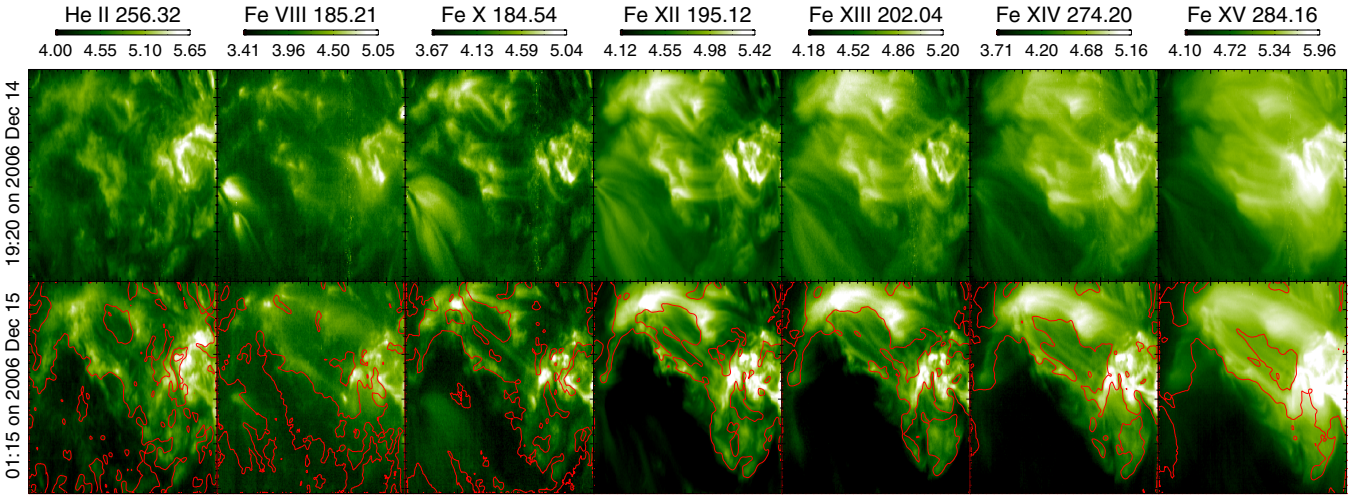

Figure 15. Intensity maps of different emission lines for the two scans starting at 19:20 on 2006 December 14 and 01:15 on 2006 December 15. The red contours outline regions where the intensity was significantly reduced ($\geqslant$20%).

(A color version of this figure is available in the online journal.)

the profiles of other selected lines. This means that the blends to Fe XII λ195.12 and Fe XIV λ274.20 were simply neglected since their contribution to the total emission is of the order of 5% or less in outer parts (low density) of ARs (see below and Young et al. 2009). The influence of the blend Al IX λ284.03 is also negligible since it is at the far wing of the Fe XV λ284.16 line and is very weak in AR conditions. The He II λ256.32 line is blended with several other higher-temperature lines (Fe XIII λ256.42, Fe XII λ256.41, and Si X λ256.37). We included this line for our DEM analysis since it is the only strong EIS line formed in the lower TR and it contributes more than 80% of the total emission in disk observations (Young et al. 2007). Moreover, the blends are all sitting at the red wing of the He II λ256.32 line profile, and their spectral distances from the He II λ256.32 line center are ~60–120 km s^{-1}. We note that in such a case our SGF algorithm mainly fits the core and blue wing of the line profile, which is primarily the emission of He II λ256.32 rather than the blends. Note that the weak, high-speed outflow was not considered in the DEM and the following density diagnostics since it only contributes a few percent to the integrated intensity of the average line profiles. We can see from Figure 16 that the main difference is the reduced emission at high temperatures ($\log(T/\mathrm{K}) = 6.1$–6.3) in the dimming region. This result seems to suggest that in this event a significant portion of the cool TR materials did not escape when the magnetic field lines opened up. A similar result has also been obtained by Robbrecht & Wang (2010) based on EUV imaging observations. We have to mention that the lower-temperature part of the DEM curves is less constrained due to the lack of many cool lines in the EIS observation. Observations of IRIS, which will be launched in

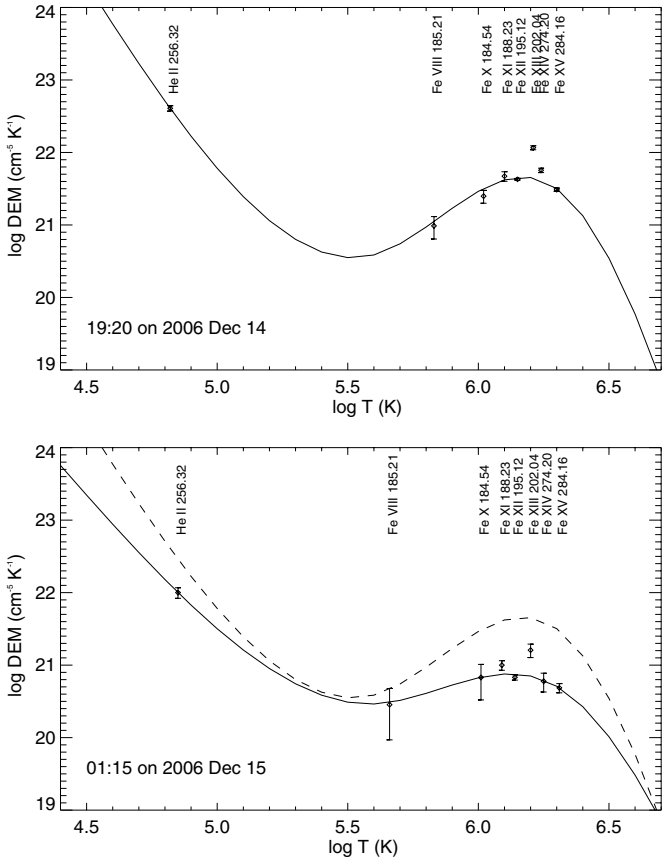

Figure 16. DEM curves for the two scans starting at 19:20 on 2006 December 14 (upper panel, before eruption) and 01:15 on 2006 December 15 (lower panel, dimming). The DEM curve before the eruption is overplotted as the dashed line in the lower panel.

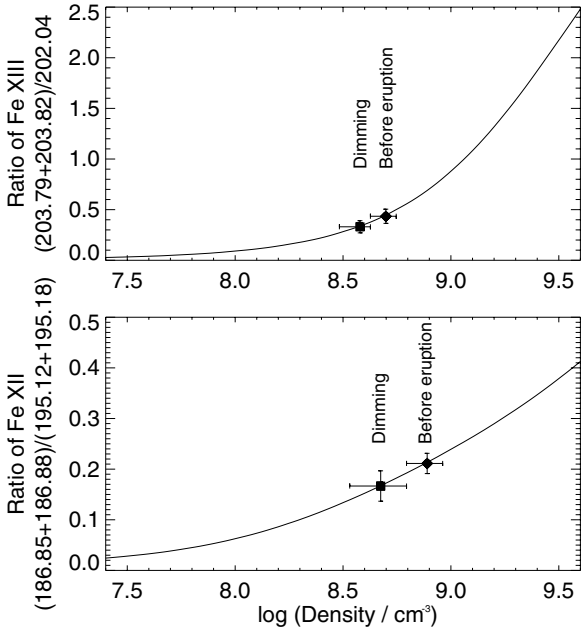

Figure 17. Relationship between electron density and line ratio, as derived from the CHIANTI database. The measured values before the eruption (15:11 on 2006 December 14) and during dimming (10:29 on 2006 December 15) are indicated by the solid diamonds and squares, respectively. The vertical and horizontal bars indicate the standard deviations of the intensity ratios and uncertainties of the calculated densities, respectively.

2012, are thus crucial since several strong cool lines are included in its spectrum.

There are several density-sensitive line pairs used in the first (15:11–16:01) and last scans (10:29–11:19) of the 2006 December 14–15 observation. Thus, we can compare the densities of the dimming region with pre-eruption densities. Line pairs Fe XII λλ186.88 and 195.12 and Fe XIII λλ203.82 and 202.04 were chosen for the density diagnostics. Fe XII λ186.88 is actually a self-blend of two Fe XII lines (λλ186.85, 186.88) and the Fe XII λ195.12 line is blended with Fe XII λ195.18 (Young et al. 2007). The S XI λ186.84 line usually contributes no more than 5% of the Fe XII λ186.88 feature and thus was ignored in our calculation (Chifor et al. 2008b). The Fe XIII λ203.82 line is a self-blend of two Fe XIII lines (λλ203.79, 203.82). We calculated the line ratios and the associated standard deviations in the obvious dimming region (defined as the region with an intensity reduction larger than 20%) of the last scan and in the corresponding region of the first scan. The theoretical relationships between the line ratios and densities, as extracted from the CHIANTI database (Dere et al. 1997; Landi et al. 2006), are presented in Figure 17. The measured values before the eruption and during dimming are indicated by the solid diamonds and squares, respectively. We can see that the average density changes from $\log(N_e/\mathrm{cm}^{-3}) = 8.89$ to $\log(N_e/\mathrm{cm}^{-3}) = 8.67$ at $\log(T/\mathrm{K}) = 6.1$, and from $\log(N_e/\mathrm{cm}^{-3}) = 8.70$ to $\log(N_e/\mathrm{cm}^{-3}) = 8.58$ at $\log(T/\mathrm{K}) = 6.2$. This density decrease, together with the fact that the dimming is seen at all temperatures, strongly suggests that the dimming is an effect of density decrease rather than temperature change.

Following Harrison & Lyons (2000) and Jin et al. (2009), we have attempted to estimate the mass losses in several well-observed dimming regions by using two different methods. The first method is just to multiply the density change and the emission volume, which is similar to the Si X method used by Harrison et al. (2003). The calculation process can be expressed as follows:

$$M = \delta N S L m_p, \quad (2)$$

where M, δN, S, L, and m_p represent the total mass loss, change of the number density, area of the dimming region, depth of the dimming region, and proton mass, respectively. The density change δN can be calculated from the line pair Fe XII λλ186.88 and 195.12, or estimated from the intensity change of Fe XII λ195.12 if the other line was not used in the scan of dimming. The use of the Fe XII λ195.12 line seems to be reasonable since from Figure 16 we can see that the most significant decrease and the DEM peak occur around $\log(T/\mathrm{K}) = 6.1$. The dimming area S is defined as the total area where the Fe XII λ195.12 intensity drops more than 20%, multiplied by the ratio of the total dimming area in simultaneous full-disk coronal images (EIT or AIA observations) and the dimming area observed by EIS. Assuming that the emission volume is as deep as it is wide, the depth of the dimming region can be calculated as $\sqrt{S}$. As mentioned by Harrison et al. (2003), the mass calculated from this method should be considered to be a reasonable figure for a comparison with the mass of the associated CME, although the Fe XII λλ186.88 and 195.12 line pair can only detect density changes at a temperature of around $\log(T/\mathrm{K}) = 6.1$.

The second method is similar to that used by Jin et al. (2009). We take the emission heights of TR lines from the VAL3C model (Vernazza et al. 1981) and coronal lines from Mariska &

Table 2
Mass Losses Estimated from Different Methods and Outflow Densities for Three Dimming Regions

Obs. ID	Scanning Period	1st Method (g)	2nd Method (g)	CME Mass (g)	Outflow Density/log (N_e/cm^{-3})
1	2006 Dec 14 19:20–21:35	1.9×10^{15}	8.0×10^{14}	3.6×10^{15}	7.0
3	2006 Dec 13 01:12–05:41	4.1×10^{15}	1.4×10^{15}	7.0×10^{15}	7.1
4	2011 Jun 21 02:51–02:56	1.1×10^{15}	5.0×10^{14}		6.8

Withbroe (1978) and then calculate the densities at these heights from an empirical relationship between height and density (Cox 2000; Jin et al. 2009). Any density-sensitive line pairs available in EIS observations are then used to derived the densities, which are then compared with and scale the model densities. Density changes at different heights can then be derived from intensity changes of corresponding EIS lines. The total mass loss is then expressed by

$$M = \sum \delta N(h_i) S(h_i) \delta h_i m_p, \quad (3)$$

where $\delta N(h_i)$ and $S(h_i)$ are the density change and dimming area, respectively, at the emission height of the ith line.

The mass losses calculated from the two methods for several well-observed dimming events are listed in Table 2. It can be seen that the mass losses estimated from different methods are 20%–60% of the CME mass calculated from LASCO white light data (Jin et al. 2009). Such results indicate that a significant part of the CME mass originates from the region where dimming occurs subsequently. We have to bear in mind that this mass loss mainly occurs during the rapid eruption phase and is not related to the weak, high-speed outflows in the long-lasting dimming regions. Thus, in principle the values of mass loss estimated from spectroscopic observations can be used to guide our identifications of CME/ICME sources. We have to mention that no strong TR lines were used in the 2011 June 21 observation so that the mass loss derived from the second method is likely to be underestimated. We think that the difference of the DEM curves before and during the dimming, as shown in Figure 16, can in principle be used to derive the mass loss of the dimming region. However, it seems that we still have to make several assumptions for the dimming depth, as well as the changes of density and temperature gradient, which are hard to evaluate. Thus, we do not make an effort in this direction and leave it open for future investigations.

Jin et al. (2009) made an effort to calculate the mass flux for the outflows in dimming regions and concluded that the total ejected mass is about one order of magnitude larger than the CME mass. The flow velocities they used were derived from an SGF to line profiles in dimming regions, and they are of the order of ~20 km s^{-1}. The density values were taken from static solar atmosphere models. The high-speed outflows we find in dimming regions can provide a significant amount of material to refill the corona since they are always there until the complete recovery of the dimming (often lasting from hours to days). If we assume that the mass refilling the corona comes from the high-speed outflows, we should expect to see an equivalence of the total mass supplied by the outflow and the mass loss in the corresponding dimming region. If we simply estimate the total mass supplied by the outflow as the product of mass flux density, area (S), and duration (t) of the dimming, we can have the following relationship:

$$\delta N S L = n v S t. \quad (4)$$

From EIT or AIA observations, we roughly estimated the duration of significant dimming as 14, 14, and 10 hr for the 2006 December 14, 2006 December 13, and 2011 June 21 events, respectively. If we take a value of 100 km s^{-1} for the speed (v), the density (n) of the outflow can then be calculated from Equation (4). The calculated densities of the outflows are listed in Table 2. These values are about two orders of magnitude smaller than the pre-eruption densities at log (T/K) = 6.1 and should only be regarded as the lower limits since some of the outflows may overcome the gravity and become part of the solar wind. The lower limit of the mass flux density associated with these high-speed outflows is thus estimated to be about 1.67×10^{-10} g cm^{-2} s^{-1} if using a density of log (N_e/cm^{-3}) = 7.0, while the average outflow mass flux density of the dimming region in the 01:15–03:30 scan on 2006 December 14 is estimated to be about 1.0×10^{-9} g cm^{-2} s^{-1} if using results of SGF, i.e., an average velocity of 12.5 km s^{-1} and a density of log (N_e/cm^{-3}) = 8.67. These values are within one order of magnitude of the mass flux density of type-I spicules (~1.67×10^{-9} g cm^{-2} s^{-1}; Pneuman & Kopp 1978), type-II spicules (~1.5×10^{-9} g cm^{-2} s^{-1}; De Pontieu et al. 2011), coronal rains (~1.14×10^{-9} g cm^{-2} s^{-1}; Antolin & Rouppe van der Voort 2012), and outflows in the quiet-Sun network (~1.6×10^{-9} g cm^{-2} s^{-1}; Tian et al. 2009).

We have to point out that the calculations of the mass flux of the high-speed outflows are mainly based on the assumption that there are only two emission components and that the primary component is at rest. However, in fact we cannot tell whether the primary component is really at rest or moving upward with a small velocity (e.g., ~10 km s^{-1}) since EIS does not allow an absolute wavelength calibration. Moreover, due to the large instrumental width, we cannot rule out the possibility of more than two components with each slightly Doppler-shifted with respect to each other (e.g., Doschek et al. 2008).

4.2. Erupted CME Loop and EUV Jet

In the case of erupted CME loops or EUV jets, since we can often unambiguously separate the ejecta emission component from the background emission component, e.g., Figures 12 and 13, in principle we should be able to diagnose the plasma properties separately for each of the two components. Using the fitting results shown in Figure 13, we calculated the DEM curves of the two components. From Figure 18, we can see that the ejecta (EUV jet) has more emission around log (T/K) = 5.5, as compared to the background. We can also see that the emitting materials of the EUV jet are almost equally distributed over the temperature range of log (T/K) = 5.4–6.1. We have to mention that there was only one line with a formation temperature of log (T/K) $\leqslant$ 5.5 (He II λ256.32) in our EIS observations so that the low-temperature part of the DEM is not well constrained. Future joint observations of EIS and IRIS are thus highly desired. Unfortunately, there are no very cool lines (with a formation temperature comparable to that of He II λ256.32) in the 2011 February 14 observation, so we could not perform a

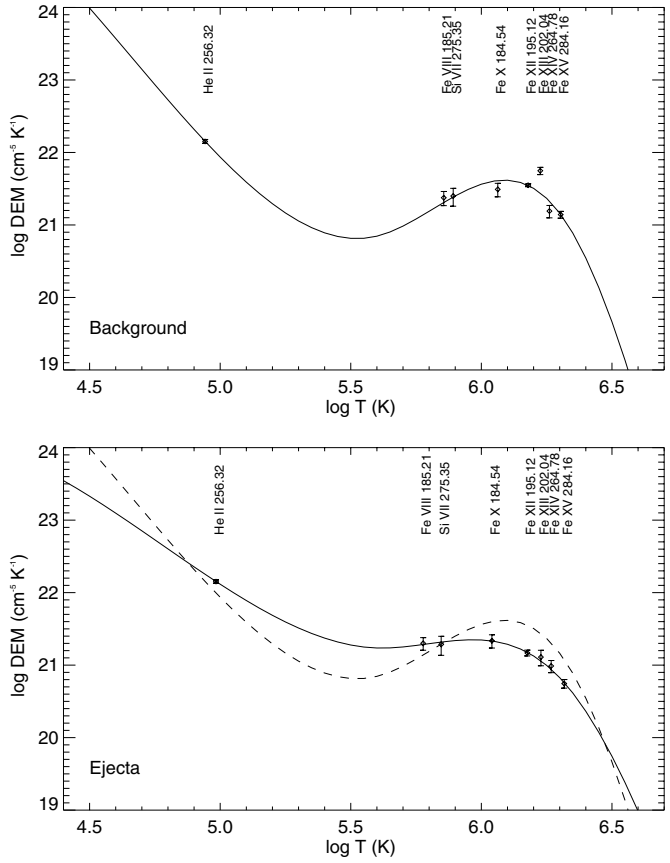

Figure 18. DEM curves of the background (upper panel, stationary component) and ejecta (lower panel, highly blueshifted component) for the rectangular region marked in Figure 6. The DEM curve of the background is overplotted as the dashed line in the lower panel.

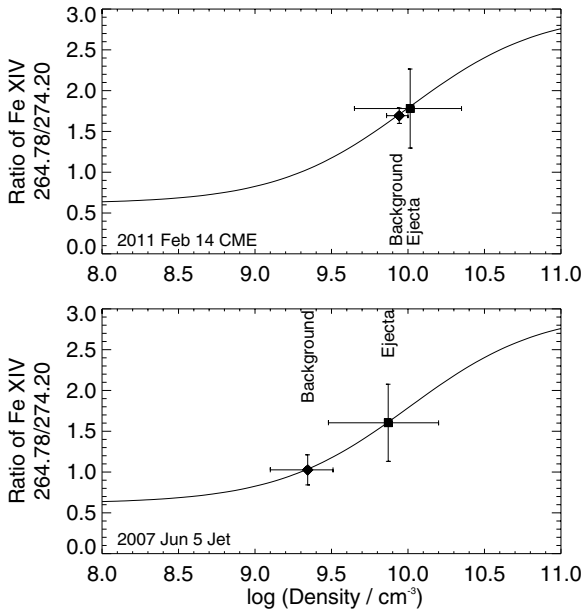

Figure 19. Relationship between electron density and line ratio, as derived from the CHIANTI database. The measured values for the emission of the background and ejecta are indicated by the solid diamonds and squares, respectively. The error bars indicate uncertainties of the ratios and densities as calculated from the 1σ uncertainties of the double Gaussian fit intensities. Upper: the 2011 February 14 CME; lower: the 2007 June 5 jet.

reliable DEM analysis (with a wide temperature coverage) for the CME ejecta in this observation.

The density-sensitive line pair Fe XIV λλ264.78 and 274.20 was included in both the 2007 June 5 and 2011 February 14 observations. The Fe XIV λ274.20 line is blended with Si VII λ274.18. The intensity of Si VII λ274.18 can be estimated from Si VII λ275.35 since the ratio of the two is at most 0.25 (Young et al. 2007). We used another observation that included both the Si VII λ275.35 and Fe XIV λ274.20 lines (Tian et al. 2011c) and estimated that the contribution of Si VII λ274.18 to the total emission is at most 5.4%. Thus, we simply ignored this blend. The theoretical relationship between the line ratio and density, and the measured values for the two components are shown in Figure 19. We can see that the measured values are in the density-sensitive part of the theoretical relationship. The ejecta, which is an EUV jet in the 2007 June 5 observation and an erupted loop in the 2011 February 14 observation, seems to have a larger density compared to the background emission. The measured densities are $\log(N_e/\mathrm{cm}^{-3}) = 9.89$ for the EUV jet and $\log(N_e/\mathrm{cm}^{-3}) = 10.01$ for the erupted CME loop. However, the uncertainties of the line ratios for the ejecta are very large. This is largely due to the fact that the ejecta component in the Fe XIV λ274.20 line profile was too close to the edge of the spectral window so that it was only partly resolved. The measured densities of the background components are consistent with (in the jet case) or about two times larger than (in the CME case) the normal AR densities at similar temperatures (Tripathi et al. 2008). To the best of our knowledge, this is the first time that the electron densities of EUV jets and erupted CME loops are measured through an unambiguous decomposition of line profiles. Unfortunately, no density-sensitive line pairs formed at lower temperatures were included in these two observations.

For the EUV jet, the total mass of the ejected material can be calculated by multiplying the mass flux density, cross-section area, and lifetime of the jet. Taking a density of $\log(N_e/\mathrm{cm}^{-3}) = 9.89$, a speed of 223 km s^{-1}, a jet width of 8″, and a lifetime of 11 minutes (Yang et al. 2011), the total ejected mass is estimated as 5.0×10^{13} g. This is about two orders of magnitude lower than the typical value of CME mass.

The mass of the erupted loop in the 2011 February 14 observation can be calculated by taking a density value of $\log(N_e/\mathrm{cm}^{-3}) = 10.01$. After estimating the loop cross-section area and loop length from the AIA 193 Å image at 19:29, the mass of the erupted loop was estimated to be 2.5×10^{14} g. Such a value is comparable to the lower limit of the typical CME mass. However, we have to bear in mind that the density value we used only represents the density of the emitting materials with a temperature around $\log(T/\mathrm{K}) = 6.25$.

We have to mention that both the DEM and density calculations are based on ionization equilibrium. In the case of flows, this equilibrium might be destroyed (Peter et al. 2006). To quantify how the flows impact the results of temperature and density diagnostics, further numerical simulations are needed.

5. CONCLUSION

We have analyzed several data sets obtained by EIS during solar eruptions such as CMEs, coronal dimmings, and EUV jets. We have mainly identified three types of flows and investigated the properties of them. We have also performed density diagnostics and DEM analyses for coronal dimmings, erupted CME loops, and EUV jets. Our analyses suggest that spectroscopic observations can provide valuable information on

the LOS kinematics and plasma properties of CMEs and EUV jets.

Previous analyses based on SGFs reveal significant blueshift and enhanced line width in the CME-induced dimming regions, which sometimes last for hours or days. However, our detailed RB asymmetry analyses and RB-guided double Gaussian fits of the coronal line profiles clearly show blueward asymmetries in dimming regions, suggesting perhaps the presence of a relatively weak (∼10% of the total emission), high-speed (∼100 km s^{-1}) upflow component superimposed on a strong background emission component. This upflow component may result from the impulsive heating in the lower solar atmosphere. We have found that both the blueshift and line width correlate very well with the blueward asymmetry, suggesting that the significant blueshift and enhanced line width are actually largely caused by the superposition of the two components. This finding suggests that a small portion of the plasma in the dimming region is flowing outward at a velocity of the order of 100 km s^{-1} and that caution must be taken when interpreting spectroscopic data. Part of these weak, high-speed outflows may provide a significant amount of mass to refill the corona after the eruption of CMEs, and the other part may become solar wind streams impacting the kinematics of CMEs. Our plasma diagnostics of the dimming region suggest that dimming is mainly an effect of density decrease rather than temperature change. The mass losses in dimming regions have been estimated from two different methods, and they are 20%–60% of the masses of the associated CMEs, suggesting that a significant part of the CME mass indeed comes from the region where dimming occurs subsequently. The mass flux carried by the outflows has also been estimated from observations.

Several temperature-dependent outflows have been found immediately outside the (deepest) dimming regions. The speed increases with temperature and reaches ∼150 km s^{-1} at log (T/K) = 6.3. Interestingly, our RB asymmetry analysis is able to detect some of these temperature-dependent outflows. These outflows are interpreted as evaporation flows, which are perhaps driven by enhanced thermal conduction or nonthermal electron beams along reconnecting field lines, or induced by the interaction between the opened field lines in the dimming region and the closed loops in the surrounding plage region.

Profiles of emission lines formed at coronal and TR temperatures clearly exhibit two well-separated components in erupted CME loops and EUV jets. Besides an almost stationary component accounting for the background emission, there is a highly blueshifted (∼200 km s^{-1}) component representing emission from the erupting material. The two components can be easily decomposed through a double Gaussian fit, and we have diagnosed the electron density, performed a DEM analysis, and estimated the mass of the ejecta. Different properties of the two components suggest the importance of separating emission from different sources when studying dynamic events. Combining the speed of the blueshifted component and the projected speed of the ejecta from simultaneous imaging observations, we have calculated the real speeds of the erupted CME loop and EUV jet.

SDO is the first mission of NASA's Living With a Star (LWS) Program. EIS is an instrument on board *Hinode*, a Japanese mission developed and launched by ISAS/JAXA, with NAOJ as domestic partner and NASA and STFC (UK) as international partners. It is operated by these agencies in cooperation with ESA and NSC (Norway). We thank the referee for his/her careful reading of the paper and for the comments and suggestions. We also appreciate the helpful discussions with R. A. Harrison and M. Zhang. S. W. McIntosh is supported by NASA (NNX08AL22G, NNX08BA99G) and NSF (ATM-0541567, ATM-0925177). L.-D. Xia and J.-S. He are supported by the National Natural Science Foundation of China (NSFC) under contracts 40931055, 40890162, 40974105, and 41174148. H. Tian is supported by the ASP Postdoctoral Fellowship Program of NCAR. The National Center for Atmospheric Research is sponsored by the National Science Foundation.

APPENDIX

PROFILE ASYMMETRIES NOT CAUSED BY BLENDS OR NOISE

The high-speed outflowing component discussed in Section 3.1 is usually much weaker than the primary component, which may prompt people to consider whether these high-speed outflows are caused by a weak blend or simply random noise. However, from the red contours in Figure 1 we can clearly see that most Fe XIII λ202.04 profiles showing significant blueward asymmetries actually have a high enough S/N. Moreover, the blueward asymmetries form patches and coincide with patches of significant blueshift and enhanced line width. If the blueward asymmetries are caused by random noise, we should see a random distribution of asymmetric line profiles in space.

The cause of the blueward asymmetries by possible blends at the blue wings of the line profiles can also be ruled out, since we see these blueward asymmetries in not only one line but all strong coronal lines in the EIS spectrum. As discussed in Section 3.1, the significant blueward asymmetries in the velocity range of 70–130 km s^{-1} at wings of these line profiles cannot be caused by identified blends.

There is another way to verify the above argument: the center-to-limb variation. We could not find any EIS observation of a coronal dimming region as it rotates from the limb to disk center. However, we do have EIS observations of ARs as they rotate from the limb to disk center. As discussed in Section 3.1, the high-speed outflows in dimming regions seem to be very similar to those in AR boundaries. We take three EIS raster scans of the AR 10978 from 2007 December 10 to 15 for an analysis. Details of these observations can be found in Bryans et al. (2010). The AR was close to the east limb, disk center, and west limb on December 10, 12, and 15, respectively. Figure 20 shows the spatial distributions of the single Gaussian parameters and profile asymmetries (averaged over the velocity interval of 70–130 km s^{-1}, as obtained from the RB_P profiles) for the three scans. Center-to-limb variations of the profile asymmetries are clearly present. When the AR was on the disk center, we see prominent blueward asymmetries at both boundaries. As the AR rotated to the west limb, the profile asymmetries disappeared at the western boundary. And the profile asymmetries almost disappeared at the eastern boundary when the AR was close to the east limb. Clearly, it is hard to explain this phenomenon by noise or blends, while our scenario, namely, a high-speed outflow superimposed on a nearly static coronal background, can easily explain this center-to-limb variation by taking into account the LOS projection effect. When the AR was close to the west limb, the magnetic field lines in the western boundary are almost perpendicular to the LOS so that the projection of the outflow speed on the LOS direction is very small, leading to a very small velocity offset between different components and greatly reduced blueward asymmetries in the velocity interval

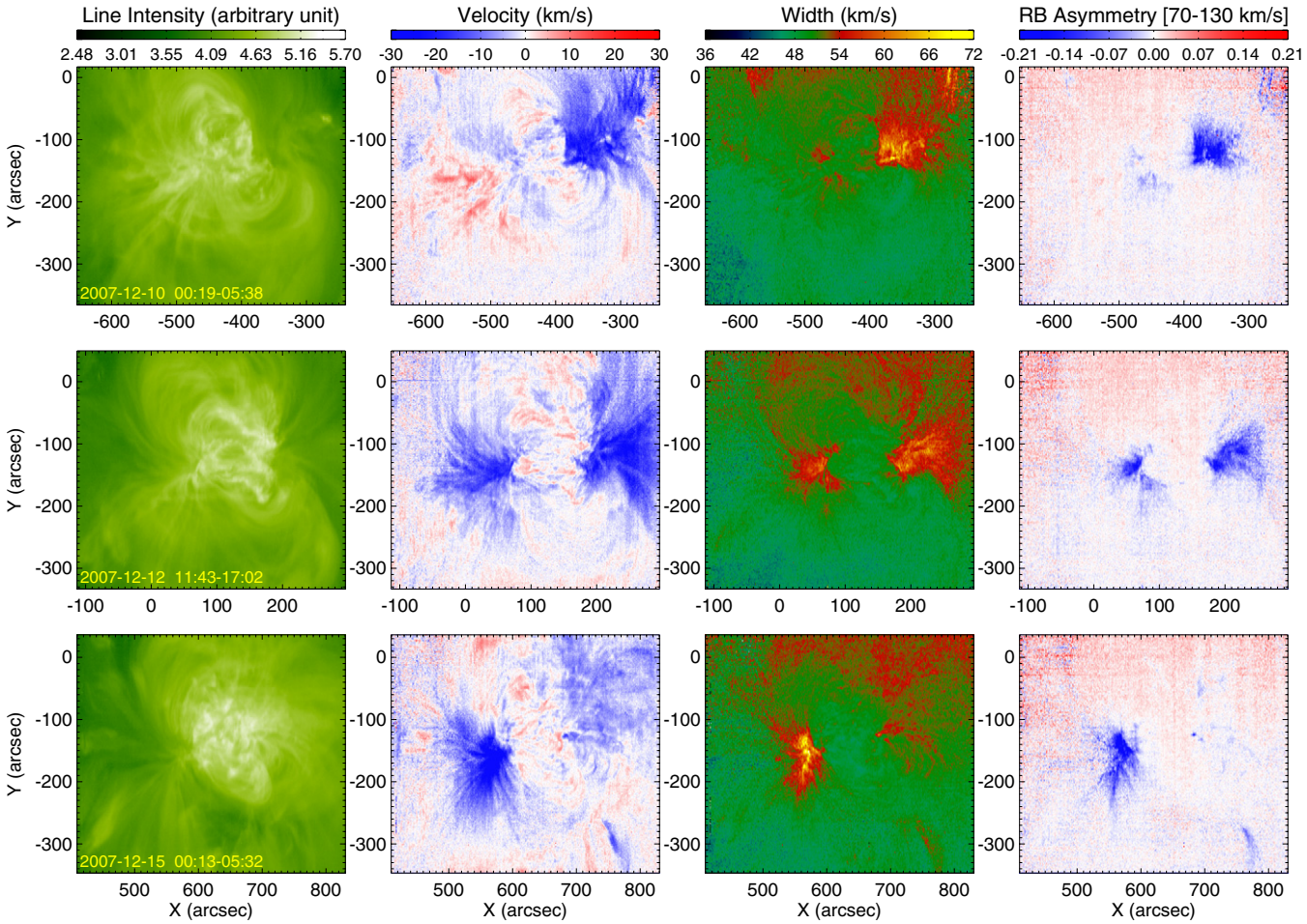

Figure 20. Spatial distributions of the single Gaussian parameters and profile asymmetries (averaged over the velocity interval of 70–130 km s^{-1}, as obtained from the RB_P profiles) for Fe XIII λ202.04 in a scan from 00:19 to 05:38 on 2007 December 10 (first row), 11:43 to 17:02 on 2007 December 12 (second row), and 00:13 to 05:32 on 2007 December 15 (third row).

(A color version of this figure is available in the online journal.)

of 70–130 km s^{-1}. This effect would also reduce the magnitude of the blueshift and line width of the total emission, as also revealed by Figure 20.

REFERENCES

Alexander, D., & Fletcher, L. 1999, Sol. Phys., 190, 167
Antiochos, S. K., & Sturrock, P. A. 1978, ApJ, 220, 1137
Antolin, P., & Rouppe van der Voort, L. 2012, ApJ, 745, 152
Asai, A., Hara, H., Watanabe, T., et al. 2008, ApJ, 685, 622
Attrill, G. D. R., Harra, L. K., van Driel-Gesztelyi, L., & Démoulin, P. 2007, ApJ, 656, L101
Attrill, G. D. R., Harra, L. K., van Driel-Gesztelyi, L., & Wills-Davery, M. J. 2010, Sol. Phys., 264, 119
Baker, D., van Driel-Gesztelyi, L., & Green, L. M. 2012, Sol. Phys., 276, 219
Berlicki, A., Heinzel, P., Schmieder, B., Mein, P., & Mein, N. 2005, A&A, 430, 679
Bewsher, D., Harrison, R. A., & Brown, D. S. 2008, A&A, 478, 897
Bocchialini, K., Baudin, F., Koutchmy, S., et al. 2011, A&A, 533, A96
Bradshaw, S. J., Aulanier, G., & Del Zanna, G. 2011, ApJ, 743, 66
Brooks, D. H., & Warren, H. P. 2011, ApJ, 727, L13
Brown, C. M., Feldman, U., Seely, J. F., & Korendyke, C. M. 2008, ApJS, 176, 511
Bryans, P., Young, P. R., & Doschek, G. A. 2010, ApJ, 715, 1012
Chae, J., Schühle, U., & Lemaire, P. 1998, ApJ, 505, 957
Chen, F., & Ding, M. D. 2010, ApJ, 724, 640
Chen, F., Ding, M.-D., & Chen, P.-F. 2010, ApJ, 720, 1254
Chen, F., Ding, M.-D., Chen, P.-F., & Harra, L. K. 2011, ApJ, 740, 116
Chen, P.-F., Innes, D. E., & Solanki, S. K. 2008, A&A, 484, 487
Cheng, X., Ding, M.-D., & Zhang, J. 2010, ApJ, 712, 1302
Chifor, C., Isobe, H., Mason, H. E., et al. 2008a, A&A, 491, 279
Chifor, C., Young, P. R., Isobe, H., et al. 2008b, A&A, 481, L57
Cox, A. N. (ed.) 2000, Allen's Astrophysical Quantities (4th ed.; New York: Springer)
Culhane, J. L., Harra, L. K., James, A. M., et al. 2007, Sol. Phys., 243, 19
Del Zanna, G. 2008, A&A, 481, L49
Del Zanna, G., Aulanier, G., Klein, K.-L., & Török, T. 2011a, A&A, 526, A137
Del Zanna, G., Berlicki, A., Schmieder, B., & Mason, H. E. 2006, Sol. Phys., 234, 95
Del Zanna, G., Mitra-Kraev, U., Bradshaw, S. J., Mason, H. E., & Asai, A 2011b, A&A, 526, A1
De Pontieu, B., & McIntosh, S. W. 2010, ApJ, 722, 1013
De Pontieu, B., McIntosh, S. W., Carlsson, M., et al. 2011, Science, 331, 55
De Pontieu, B., McIntosh, S. W., Hansteen, V. H., & Schrijver, C. J. 2009, ApJ, 701, L1
Dere, K. P., Landi, E., Mason, H. E., Monsignori-Fossi, B. C., & Young, P. R. 1997, A&AS, 125, 149
De Toma, G., Holzer, T. E., Burkepile, J. T., & Gilbert, H. R. 2005, ApJ, 621, 1109
Ding, J. Y., Madjarska, M. S., Doyle, J. G., et al. 2011, A&A, 535, A95
Dolla, L. R., & Zhukov, A. N. 2011, ApJ, 730, 113
Doschek, G. A., Mariska, J. T., Warren, H. P., et al. 2007, ApJ, 667, L109
Doschek, G. A., Warren, H. P., Mariska, J. T., et al. 2008, ApJ, 686, 1362
Fan, Y. 2011, ApJ, 740, 68
Feng, X. S., Zhang, Y., Yang, L. P., Wu, S. T., & Dryer, M. 2009, J. Geophys. Res., 114, A10103
Gopalswamy, N., & Hanaoka, Y. 1998, ApJ, 498, L179
Gosling, J. T., McComas, D. J., Philips, J. L., & Bame, S. J. 1991, J. Geophys. Res., 96, 7831
Graham, D. R., Fletcher, L., & Hannah, I. G. 2011, A&A, 532, A27

Hansteen, V. H., Hara, H., De Pontieu, B., & Carlsson, M. 2010, ApJ, 718, 1070
Hara, H., Watanabe, T., Harra, L. K., et al. 2008, ApJ, 678, L67
Hara, H., Watanabe, T., Harra, L. K., et al. 2011, ApJ, 741, 107
Harra, L. K., Hara, H., Imada, S., et al. 2007, PASJ, 59, S801
Harra, L. K., Mandrini, C. H., Dasso, S., et al. 2011a, Sol. Phys., 268, 213
Harra, L. K., Sakao, T., Mandrini, C. H., et al. 2008, ApJ, 676, L147
Harra, L. K., & Sterling, A. C. 2001, ApJ, 561, L215
Harra, L. K., & Sterling, A. C. 2003, ApJ, 587, 429
Harra, L. K., Sterling, A. C., Gömöry, P., & Veronig, A. 2011b, ApJ, 737, L4
Harrison, R. A., & Bewsher, D. 2007, A&A, 461, 1155
Harrison, R. A., Bryans, P., Simnett, G. M., & Lyons, M. 2003, A&A, 400, 1071
Harrison, R. A., & Lyons, M. 2000, A&A, 358, 1097
Harrison, R. A., Sawyer, E. C., Carter, M. K., et al. 1995, Sol. Phys., 162, 233
He, J.-S., Marsch, E., Curdt, W., et al. 2010a, A&A, 519, A49
He, J.-S., Marsch, E., Tu, C.-Y., Guo, L.-J., & Tian, H. 2010b, A&A, 516, A14
Hudson, H. S., Lemen, J. R., St. Cyr, O. C., Sterling, A. C., & Webb, D. F. 1998, Geophys. Res. Lett., 25, 2481
Imada, S., Hara, H., Watanabe, T., et al. 2007, PASJ, 59, S793
Imada, S., Hara, H., Watanabe, T., et al. 2011, ApJ, 743, 57
Innes, D. E., Curdt, W., Schwenn, R., et al. 2001, ApJ, 549, L249
Jiang, Y., Ji, H., Wang, H., & Chen, H. 2003, ApJ, 597, L161
Jin, M., Ding, M.-D., Chen, P.-F., Fang, C., & Imada, S. 2009, ApJ, 702, 27
Jing, J., Wiegelmann, T., Suematsu, Y., Kubo, M., & Wang, H. 2008, ApJ, 676, L81
Judge, P. G., De Pontieu, B., McIntosh, S. W., & Olluri, K. 2012, ApJ, 746, 158
Kamio, S., Hara, H., Watanabe, T., & Curdt, W. 2009, A&A, 502, 345
Kamio, S., Hara, H., Watanabe, T., et al. 2007, PASJ, 59, S757
Kim, Y.-H., Moon, Y.-J., Park, Y.-D., et al. 2007, PASJ, 59, S763
Kubo, M., Yokoyama, T., Katsukawa, Y., et al. 2007, PASJ, 59, 779
Landi, E., Del Zanna, G., Young, P. R., et al. 2006, ApJS, 162, 261
Lee, K.-S., Moon, Y.-J., Kim, S.-J., et al. 2011, ApJ, 736, 15
Lemaire, P., Wilhelm, K., Curdt, W., et al. 1997, Sol. Phys., 170, 105
Lemen, J. R., Title, A. M., Akin, D. J., et al. 2012, Sol. Phys., 275, 17
Li, Y., & Ding, M.-D. 2009, Res. Astron. Astrophys., 9, 829
Li, Y., & Ding, M.-D. 2011, ApJ, 727, 98
Li, Y., & Ding, M.-D. 2012, Res. Astron. Astrophys., in press (arXiv:1111.4235)
Lin, C.-H., Banerjee, D., OShea, E., & Doyle, J. G. 2006, A&A, 450, 1181
Liu, C., Deng, N., Liu, R., et al. 2011, ApJ, 735, L18
Liu, R., Wang, T.-J., Lee, J., et al. 2011, Res. Astron. Astrophys., 11, 1209
Liu, Y., Thernisien, A., Luhmann, J. G., et al. 2010, ApJ, 722, 1762
Madjarska, M. S., Doyle, J. G., Innes, D. E., & Curdt, W. 2007, ApJ, 670, L57
Mandrini, C. H., Nakwacki, M. S., Attrill, G., et al. 2007, Sol. Phys., 244, 25
Mariska, J. T., & Withbroe, G. L. 1978, Sol. Phys., 60, 67
Marsch, E., Tian, H., Sun, J., Curdt, W., & Wiegelmann, T. 2008, ApJ, 685, 1262
Marsch, E., Wiegelmann, T., & Xia, L. D. 2004, A&A, 428, 629
Martínez-Sykora, J., De Pontieu, B., Hansteen, V., & McIntosh, S. W. 2011, ApJ, 732, 84
McIntosh, S. W. 2009, ApJ, 693, 1306
McIntosh, S. W., & De Pontieu, B. 2009a, ApJ, 706, L80
McIntosh, S. W., & De Pontieu, B. 2009b, ApJ, 707, 524
McIntosh, S. W., de Pontieu, B., & Leamon, R. J. 2010, Sol. Phys., 265, 5
McIntosh, S. W., Leamon, R. J., Davey, A. R., & Wills-Davey, M. J. 2007, ApJ, 660, 1653
McIntosh, S. W., Leamon, R. J., & De Pontieu, B. 2011, ApJ, 727, 7
Miklenic, C., Veronig, A. M., Temmer, M., et al. 2011, Sol. Phys., 273, 125
Milligan, R. O. 2011, ApJ, 740, 70
Milligan, R. O., & Dennis, B. R. 2009, ApJ, 699, 968
Milligan, R. O., Gallagher, P. T., Mathioudakis, M., & Keenan, F. P. 2006a, ApJ, 642, L169
Milligan, R. O., Gallagher, P. T., Mathioudakis, M., et al. 2006b, ApJ, 638, L117
Murray, M. J., Baker, D., van Driel-Gesztelyi, L., & Sun, J. 2010, Sol. Phys., 261, 253
Nishizuka, N., & Harra, H. 2011, ApJ, 737, L43
Peter, H. 2010, A&A, 521, A51
Peter, H., Gudiksen, B., & Nordlund, Å. 2006, ApJ, 638, 1086
Pneuman, G. W., & Kopp, R. A. 1978, Sol. Phys., 57, 49
Reinard, A. A., & Biesecker, D. A. 2008, ApJ, 674, 576
Robbrecht, E., & Wang, Y.-M. 2010, ApJ, 720, L88
Roussev, I., Doyle, J. G., Galsgaard, K., & Erdélyi, R. 2001, A&A, 380, 719
Rust, D. M., & Hildner, E. 1976, Sol. Phys., 48, 381
Scott, J. T., & Martens, P. C. H. 2011, ApJ, 742, 101
Shen, Y., Liu, Y., Su, J., & Deng, Y. 2012, ApJ, 745, 164
Shen, Y., Liu, Y., Su, J., & Ibrahim, A. 2011, ApJ, 735, L43
Shimojo, M., Shibata, K., Yokoyama, T., & Hori, K. 2001, ApJ, 550, 1051
Song, P., & Vasyliūnas, V. M. 2011, J. Geophys. Res., 116, A09104
Srivastava, A. K., & Murawski, K. 2011, A&A, 534, A62
Sterling, A. C., & Hudson, H. S. 1997, ApJ, 491, L55
Teriaca, L., Falchi, A., Cauzzi, G., et al. 2003, ApJ, 588, 596
Thompson, B. J., Cliver, E. W., Nitta, N., Delannée, C., & Delaboudinière, J.-P. 2000, Geophys. Res. Lett., 27, 1431
Thompson, B. J., Plunkett, S. P., Gurman, J. B., et al. 1998, Geophys. Res. Lett., 25, 2465
Tian, H., Marsch, E., Curdt, W., & He, J. 2009, ApJ, 704, 883
Tian, H., McIntosh, S. W., & De Pontieu, B. 2011a, ApJ, 727, L37
Tian, H., McIntosh, S. W., De Pontieu, B., et al. 2011b, ApJ, 738, 18
Tian, H., McIntosh, S. W., Habbal, S. R., & He, J.-S. 2011c, ApJ, 736, 130
Tripathi, D., Mason, H. E., Dwivedi, B. N., del Zanna, G., & Young, P. R. 2009, ApJ, 694, 1256
Tripathi, D., Mason, H. E., Young, P. R., & Del Zanna, G. 2008, A&A, 481, L53
Ugarte-Urra, I., & Warren, H. 2011, ApJ, 730, 37
Vernazza, J. E., Avrett, E. H., & Loeser, R. 1981, ApJS, 45, 635
Veronig, A. M. 2011, ApJ, 743, L10
Wang, T., Sui, L., & Qiu, J. 2007, ApJ, 661, L207
Wang, Y.-M., Xue, X.-H., Shen, C.-L., et al. 2006, ApJ, 646, 625
Wang, Y.-M., Ye, P.-Z., Wang, S., Zhou, G.-P., & Wang, J.-X. 2002, J. Geophys. Res., 107, 1340
Warren, H. P., Ugarte-Urra, I., Young, P. R., & Stenborg, G. 2011, ApJ, 727, 58
Watanabe, T., Hara, H., Sterling, A. C., & Harra, L. K. 2010, ApJ, 719, 213
Webb, D. F., Lepping, R. P., Burlaga, L. F., et al. 2000, J. Geophys. Res., 105, 27251
Wilhelm, K., Curdt, W., Marsch, E., et al. 1995, Sol. Phys., 162, 189
Wilhelm, K., Dammasch, I. E., & Hassler, D. M. 2002, Ap&SS, 282, 189
Yang, L.-H., Jiang, Y.-C., Yang, J.-Y, et al. 2011, Res. Astron. Astrophys., 11, 1229
Yang, S.-H., Zhang, J., Li, T., & Liu, Y. 2011, ApJ, 732, L7
Yokoyama, T., & Shibata, K. 1995, Nature, 375, 42
Young, P. R., Del Zanna, G., Mason, H. E., et al. 2007, PASJ, 59, S857
Young, P. R., O'Dwyer, B., & Mason, H. E. 2012, ApJ, 744, 14
Young, P. R., Watanabe, T., Hara, H., & Mariska, J. T. 2009, ApJ, 495, 587
Zarro, D. M., Sterling, A. C., Thompson, B. J., Hudson, H. S., & Nitta, N. 1999, ApJ, 520, L139
Zhang, J., Li, L., & Song, Q. 2007, ApJ, 662, L35
Zhang, M., & Low, B. C. 2005, ARA&A, 43, 103
Zhou, G.-P., Wang, J.-X., & Cao, Z.-L. 2003, A&A, 397, 1057